Citation
Xie, G. and Zhang, X. and Hao, H. and Shi, T. and Cui, L. and Thomas, J. 2023. Behaviour of reinforced mortarless interlocking brick wall under cyclic loading. Engineering Structures. 283 (15). http://doi.org/10.1016/j.engstruct.2023.115890

Behaviour of Reinforced Mortarless Interlocking Brick Wall under Cyclic Loading

Guanyu Xie[1], Xihong Zhang[1,*], Hong Hao[1], Tingwei Shi[1], Liuliang Cui[1], Joyis Thomas[2]

1 Centre for Infrastructural Monitoring and Protection, School of Civil and Mechanical Engineering, Curtin University, Bentley, WA 6102, Australia

2 Tetraloc Pty Ltd, Bellevue, WA 6056, Australia

*xihong.zhang@curtin.edu.au

Abstract Interlocking brick masonry has gained much attention due to its high construction efficiency and low labour skill requirement. Most designs of interlocking bricks only use interlocking keys to provide alignment for easy construction, and most previous studies of interlocking masonry structures concentrate on their static loading capacities. This study examines the behaviour of reinforced mortarless interlocking brick walls under cyclic loading. Interlocking brick wall made of a specific type of interlocking bricks with large keys that provide not only alignment in construction but also shear resistance is constructed and tested under in-plane cyclic loading. A detailed numerical model is generated and validated with the testing data, which is then used to assist the analysis of wall responses. The damage mode, hysteresis response and energy dissipation characteristics are analysed. The test results are compared with conventional masonry wall from literature to demonstrate the superior performance of interlocking masonry wall in resisting seismic loading and dissipating seismic energy. The influences of axial precompression and shear span-to-length ratio are investigated via numerical modelling.

Keywords: interlocking brick, cyclic test, mortarless, shear strength, ductility, seismic performance

1 Introduction

Masonry structures are commonly used for low- and mid-rise structures because of their cost effectiveness and outstanding sound and thermal insulation properties [1-3]. However, due to their relatively low shear strength, low ductility and poor energy dissipation capability, masonry structures are vulnerable to earthquake loading. Many masonry structure damages in earthquakes have been reported [4-6]. Intensive researches have also been conducted to improve the seismic resistance of masonry structures.

Interlocking masonry using mortarless construction method has been popularly adopted in the field of construction recently. Interlocking masonry units could self-align, which interconnect through the mechanical interlocking tenons and mortises [7]; therefore, by simply dry-stacking the masonry units on each other, the construction can be accelerated [8] while the requirement for labour skill is substantially reduced [9]. Furthermore, many types of developed interlocking masonry units, including the one used in this study, are made of compressed earth [10-14], which could bring over 18 percent cost saving compared to concrete masonry units [15]. With improved construction efficiency and reduced construction cost, there is an increasing number of applications using mortarless interlocking masonry structures especially in the rural areas of developing, as well as developed countries [10, 12, 16].

Aside from the aforementioned advantages of construction efficiency, compared to conventional masonry which relies on mortar bonding thus having low shear strength [17], interlocking masonry can provide improved shear resistance through interlocking keys. Sturm et al. [18] carried out shear tests on mortarless interlocking blocks made of rammed earth. It was found that even relatively shallow interlocking keys on the blocks improve their shear strength significantly. Furthermore, relative sliding between the dry-stacked interlocking bricks was also observed which contributes to dissipating imposed energy [19]. Through quasi-static cyclic tests, Lin et al. [20, 21] demonstrated that a significant amount of energy could be dissipated by inter-brick friction in an infill wall made of mortarless interlocking bricks.

Despite abundant research on the seismic performance of conventional mortar-bonded masonry walls [22-26], the study on the seismic performance of mortarless interlocking masonry walls is very limited. A few studies of the response of mortarless interlocking masonry walls under cyclic loading have been reported. For example, Bland [27] conducted in-plane cyclic tests on reinforced interlocking compressed earth block (ICEB) walls. It was found that the shear strength of the ICEB wall depends largely on the grouted core area rather than the interlocking mechanism; the formula to predict the shear strength of conventional masonry walls overestimates the capacity of the ICEB wall. Qu et al. [28] conducted cyclic tests on mortarless ICEB walls with substantial amount of transverse reinforcements. The influences of aspect ratio, wall flange and window opening on the lateral strength and ductility were investigated. However, the influence of the interlocking mechanism was not investigated. Kohail et al. [29] conducted quasi-static in-plane cyclic loading tests on reinforced masonry walls made of three types of blocks, i.e., conventional masonry blocks (with mortar bonding between blocks), dry-stacked Azar blocks, and dry-stacked Sparlock blocks. The lateral strength of the mortarless Azar block wall proved similar to that of the conventional block wall, but the mortarless Sparlock blocks showed much poorer lateral strength compared to the conventional block wall, indicating the pronounced influence of interlocking key shapes on the seismic performance of interlocking masonry walls. Liu et al. [19] conducted cyclic loading tests on small-scale assemblies of mortarless bricks with different interlocking key shapes and focused on the friction coefficients and energy dissipation between bricks under different axial loading levels. However, the interlocking bricks used in their study only had out-of-plane shear resistance and hence provided negligible strength enhancement in the in-plane direction. Similarly, Gul et al. [12, 30] conducted cyclic tests on unconfined and confined mortarless masonry structures made of Hydraform blocks, a type of interlocking blocks that only interlock in the out-of-plane direction as well. It was found that the concrete confining elements could effectively restrain the in-plane free sliding of the interlocking blocks and led to significant ductility and lateral strength improvement of the structure. However, at high storey drifts, block sliding led to much severe confining frame damages. Overall, these studies mostly focused on particular

types of interlocking masonry units, where the interlocking tenons and mortises were either primarily designed for improving the self-alignment and were hence relatively small, thus providing small shear resistance enhancement, or only provide shear resistance in the out-of-the-plane direction. Although large shear keys that can interlock in both the out-of-plane and in-plane directions have been shown to effectively improve the static and dynamic shear performance of precast segmental columns [31-33], when it comes to masonry structures, heretofore there have been very limited studies on the in-plane cyclic performance of walls made of interlocking bricks with relatively large shear keys that can provide both in-plane and out-of-the-plane resistance, besides alignment. Shaking table tests have been performed on interlocking masonry structures. For instance, Elvin and Uzoebgo performed laboratory shaking table tests on a mortarless masonry structure made of Hydraform interlocking bricks [34, 35]. Wide-spread inter-brick movements were observed, which dissipated much energy through friction. However, as in [12, 19, 30], the Hydraform bricks did not interlock in the in-plane direction and thus did not provide significant shear strength improvement under in-plane seismic loading. Ali [36] and Ali et al. [37] conducted shaking table tests on interlocking block walls with and without post-tensioned reinforcement. The blocks provided interlocking in both in-plane and out-of-plane directions. Nevertheless, no mass or axial loading was placed on top of the tested walls; hence, the results obtained in the tests could not be extended to more practical situations. Xie et al. [38, 39] conducted shaking table tests on mortarless masonry wall made of the same type of interlocking bricks as used in this study. Significant rocking response and toe crushing instead of diagonal shear cracking were observed, which is a result of the high shear strength and the weak vertical tensile strength of interlocking brick structures.

Overall, to the authors' best knowledge, there is very limited research on the cyclic performance of mortarless interlocking masonry walls made of bricks with large, shear-resistant interlocking keys. In this study, the behaviour of mortarless interlocking masonry walls made of a specific type of interlocking bricks with large shear keys under in-plane cyclic loading is investigated. Laboratory cyclic test is conducted on a reinforced mortarless interlocking brick wall. Compared to the wall made of the same type of interlocking

bricks in the shaking table test [38, 39], the vertical reinforcement is strongly anchored to the footing to prevent severe rocking response of the wall; the shear strength provided by the large interlocking keys could therefore be utilised to a greater extent. Then, a detailed finite element model is generated, which is validated with the testing data. The damage mode, hysteresis response and energy dissipation characteristic are analysed. Comparisons are made between the tested mortarless interlocking brick wall and a conventional masonry wall from literature on their failure modes and hysteresis responses. The influences of axial precompression and shear span-to-length ratio on mortarless interlocking brick wall responses are investigated by numerical simulations.

2 Laboratory Cyclic Loading Test

2.1 Details of the interlocking bricks

Figure 1 illustrates the interlocking bricks used in this study. The front part of the brick (Figure 1c) is featured with four interlocking keys; the rear part (Figure 1d) has two interlocking keys. Strong interlocks are developed between adjacent bricks by those keys in both the in-plane and out-of-plane directions [10, 40]. Two 30mm-diameter holes are designed in each brick for reinforcement bars, as shown in Figure 1b.

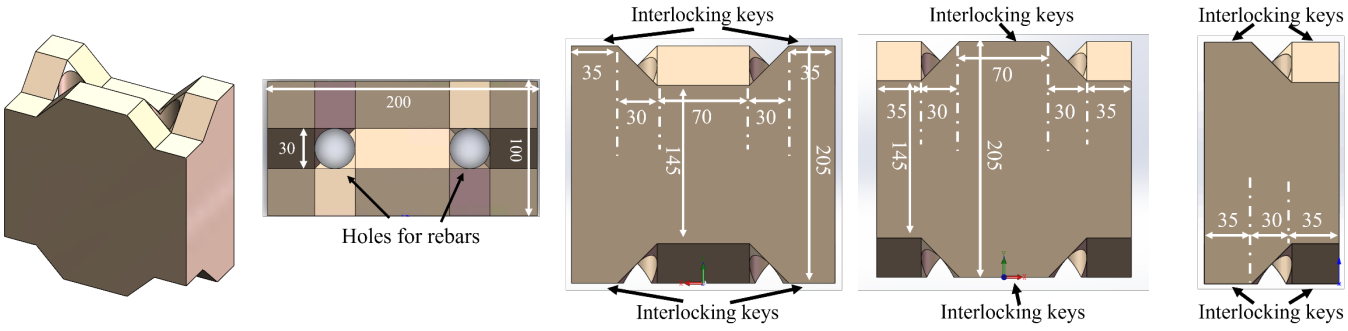

a) An interlocking brick b) Top view c) Front view d) Rear view e) Left view

Figure 1 Geometry and dimension of the full-scale interlocking bricks (unit: mm)

The interlocking bricks are made of rammed earth composed of quarry sand, aggregates, cement, and dry sand. The average density of the material is 2400kg/m^3. Uniaxial compressive tests on cylinders of the

material after 28-day curing give an average compressive strength of 20MPa with a corresponding average strain of 0.0056 and an average elastic modulus of 6700MPa. The tensile strength is assumed to be 1/10 of the compressive strength [41, 42].

2.2 Test setup and instrumentation

The in-plane cyclic loading test is set up (Figure 2a) and carried out in the Structural Dynamics Laboratory of Curtin University. An interlocking brick wall with a height of 2125mm, a length of 2400mm, and a thickness of 100mm is constructed using mortarless method on top of a reinforced concrete footing, which is fully clamped onto the strong floor. An axial pre-compression force is applied on top of the interlocking brick wall by two vertical hydraulic jacks. It results in approximately 0.47MPa axial stress on the interlocking brick wall, corresponding to the dead load on the wall in the first storey of a three- to four-storey masonry building [43]. To uniformly distribute the applied axial load throughout the cross section of the masonry wall, a steel load-transfer beam, composed of a 250UB 25.7 beam and a 250UC 72.9 beam which are welded together, is built and connected to the lower end of the jacks. Below the load-transfer beam, a reinforced concrete beam is used to connect the steel beam and the interlocking brick wall. The top concrete beam, the interlocking brick wall, and the concrete footing are connected together using four threaded D500N reinforcing bars (with a nominal diameter of 20mm and a length of 3125mm) through the pre-cast holes in the bricks, the top concrete beam and the footing. The cross-section and front view of the wall including the reinforcing bar layout are displayed in Figure 2b~c. To prevent the local damage of concrete around the anchorage points and the subsequent anchorage failure, a steel ring with an outer diameter of 120mm, an inner diameter of 27mm and a thickness of 10mm is buried in the concrete at each anchorage location. Then, the rebar is inserted through the hole of the ring and bolted at the end. As the relative movement between bricks is supposed to help the energy dissipation of the wall, the rebars are not grouted to avert the possible restraint to inter-brick movements from the grout. To avoid out of plane buckling, roller bracings are installed on both sides of the wall. The lateral loading is applied on the top of the wall through the concrete load-transfer beam.

As shown in Figure 2c, the distance between the loading point and the bottom of the wall, i.e., the shear span, is 2500mm. A servo-controlled hydraulic actuator with a stroke range of ±250mm and a loading capacity of 1000kN is used to apply the cyclic loading.

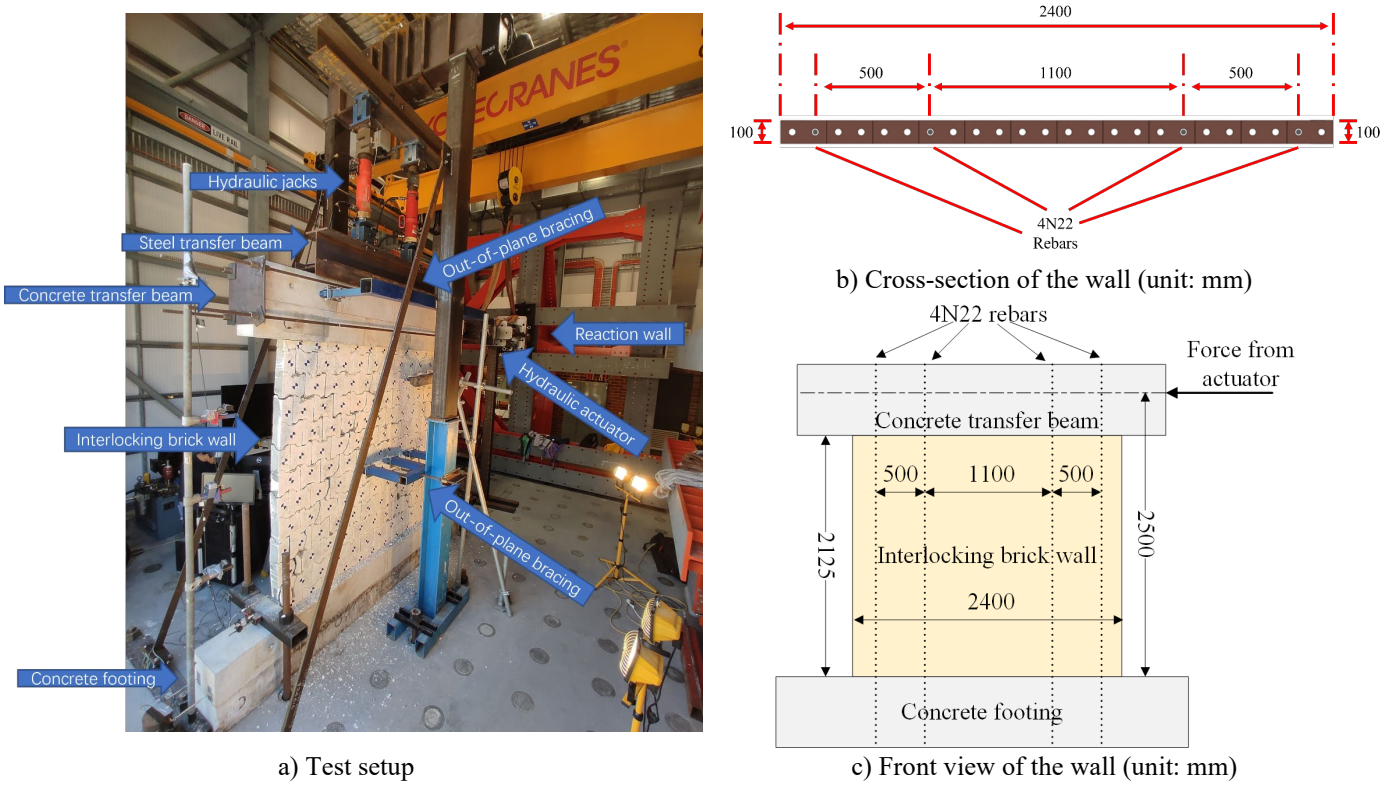

a) Test setup

b) Cross-section of the wall (unit: mm)

c) Front view of the wall (unit: mm)

Figure 2 Test setup and wall construction

Figure 3a illustrates the measurement instrumentation layout in the test. Load cells are installed on each hydraulic jack to monitor the applied axial force during the test. One in-built load cell on the horizontal actuator is used to record the applied cyclic load. Four laser linear variable differential transformers (LVDTs) are instrumented at one-quarter height, mid-height, three-quarter height of the wall and the top concrete beam, respectively, to measure the in-plane horizontal displacements of the wall at different locations. Another two LVDTs are installed on the concrete footing and the wall bottom to monitor potential sliding. For in-plane displacements, the direction where the actuator pulls the wall is defined as positive; the direction where the actuator pushes the wall is negative (Figure 3a). Additionally, two LVDTs are installed on the top beam

perpendicular to the wall plane to monitor potential wall twisting. All the instrumentation is connected to an HBM data logger. High-definition cameras are also used to monitor the damage-to-failure process of the wall during the test. For digital image correlation (DIC) analysis, the wall is painted in white with black dots, and a black-and-white tag is sticked on each brick (Figure 3b) to help track the in-plane movement of each brick.

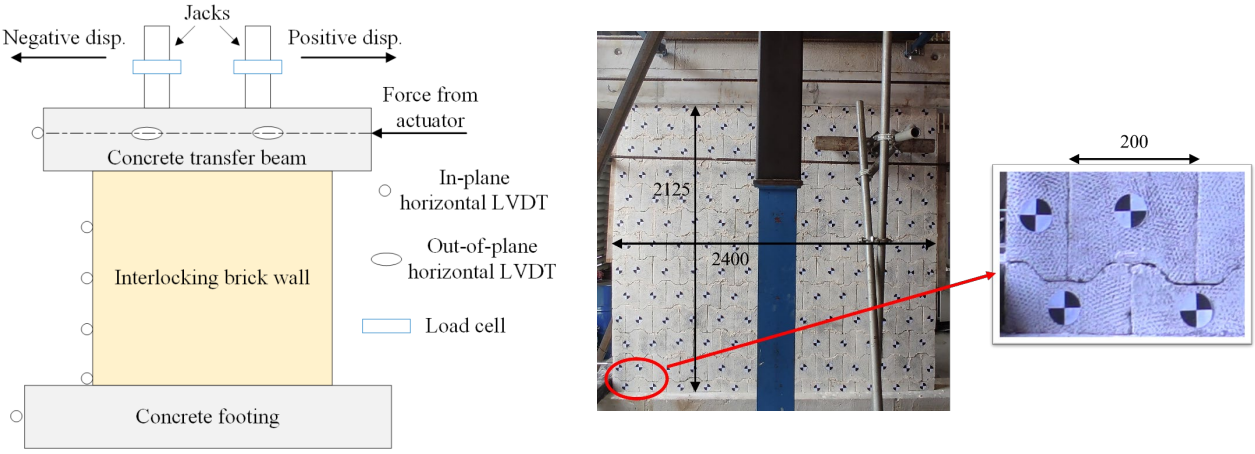

a) Instrumentation b) DIC and tracking patterns (unit: mm)

Figure 3 Instrumentation

2.3 Test procedures

The cyclic test is carried out in two steps. Firstly, the axial precompression is slowly applied by the two hydraulic jacks to the wall, which is carefully monitored to ensure the forces on the two jacks are equal. Then, horizontal cyclic loading is applied using the hydraulic actuator with displacement-controlled method. The horizontal displacement is applied slowly in reversed cycles in a sinusoidal form. Each amplitude is repeated twice following FEMA 461 [44]. The pulling direction is defined as positive. The amplitude of the cyclic loading increases gradually from 4mm to 70mm, which corresponds to the wall drift ratios from 0.19% to 3.29%. The displacement history is summarised and depicted in Table 1 and Figure 4. With the increase of the displacement amplitudes, the loading speed is gradually increased to keep the period of each loading cycle constant, with a loading speed of 0.58mm/s as the upper limit. Such a quasi-static loading scheme is suggested by Tomaževič [45] and Howlader et al. [43]. The test stops when the recorded horizontal load reduces to 80% of the maximum load achieved in the test [46, 47].

Table 1 Loading protocol

Displacement (mm)	Drift ratio (%)	Loading speed (mm/s)	Period (s)
4	0.19%	0.03	480
6	0.28%	0.05	480
10	0.47%	0.08	480
20	0.94%	0.17	480
30	1.41%	0.25	480
40	1.88%	0.33	480
50	2.35%	0.42	480
60	2.82%	0.5	480
70	3.29%	0.58	480

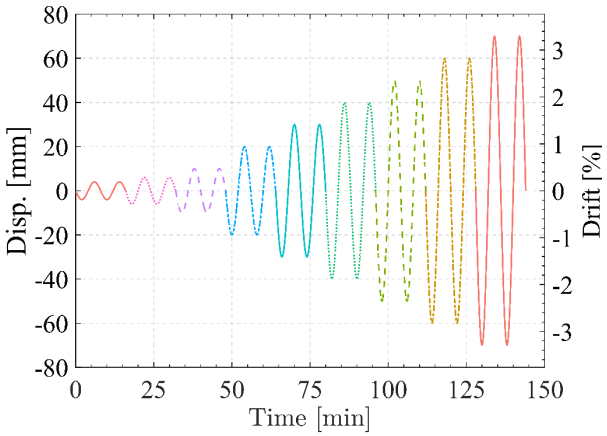

Figure 4 Loading protocol

3 Results and Analysis

The hysteresis response of the mortarless interlocking brick wall under in-plane cyclic loading is firstly presented. Then, the damage mode and the energy dissipation capacity are analysed.

3.1 Hysteretic curves

The hysteresis response of the brick wall is shown in Figure 5. During the initial loading cycles, the load increases linearly with the increase of displacement. At higher displacement levels, the lateral load in each loop increases at a lower rate, and the width of hysteresis loops gradually increases, indicating brick wall damage. Residual displacements as well as slight pinching behaviour are observed, which denote the existence of inter-brick sliding. Similar phenomena were also observed by Bland [27] and Xie et al. [38, 39]. The peak lateral load at each loop continues to increase with displacement until reaching 120kN in the pulling direction

when one reinforcing bar ruptures and the load plummets to 43kN, a significant drop by over 20% of the maximum force, indicating a near-collapse limit state according to [46]. The test is therefore terminated. An associated lateral displacement of 70mm (a drift of 3.29%) is measured at this instance. It is noted that the hysteretic curves are not perfectly symmetrical in the pushing and pulling directions because of the asymmetrical damage of the interlocking brick wall.

The backbone curve is also sketched in Figure 5, where apparent two stages can be observed, i.e., the initial linear elastic stage and the secondary elastic-plastic stage. When the lateral displacement is less than 4mm (a drift ratio of 0.19%), the wall exhibits a linear elastic behaviour. The elastic stiffness is around 10kN/mm, and the yield strength is around 40kN. As the lateral displacement increases beyond 4mm, the wall enters the elastic-plastic stage. The tangent stiffness of the backbone curve therefore reduces significantly. With the increase of displacement, the lateral force continues to increase until the reinforcing bar ruptures at the displacement of 70mm (a drift of 3.29%); the corresponding lateral load is 120kN. The ultimate load is 2.5 times that of the yield one; the corresponding displacement is 17.5 times that of the yield displacement. It demonstrates that the interlocking brick wall has a high ultimate strength and an outstanding deformation capability.

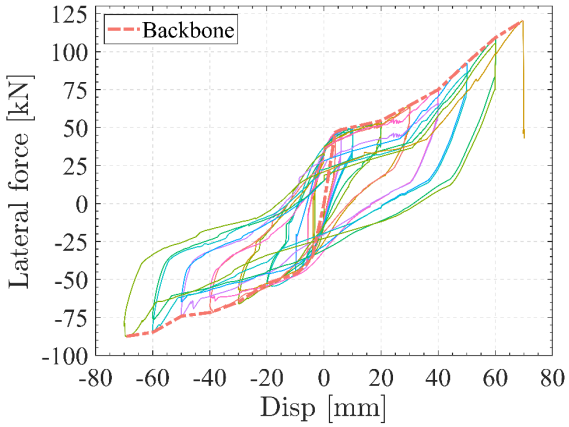

Figure 5 Hysteresis response and backbone curve

3.2 Damage evolution and failure mode

Figure 6 illustrates the vertical displacement contour of the wall through DIC technique where only the left portion of the wall is shown considering the geometric symmetry of the wall although the damage mode is not exactly symmetric. When the wall is subjected to low lateral displacement (Figure 6b~c), distinct discontinuous vertical displacement can be observed, which indicates detachment between the upper-right and lower-left bricks. Since there is no bonding strength between the mortarless interlocking bricks, this detachment occurs because the overturning moment due to the lateral load surpasses the resisting moment provided by gravity force and axial pre-compressive load. It reflects slight rocking response of the bricks and wall under lateral loading. Therefore, a stiffness reduction occurs to the mortarless interlocking brick wall at the relatively low displacement even though no significant material damage occurs. This aligns with previous studies that the lateral stiffness of walls will be reduced when rocking response occurs [48, 49]. As the applied lateral displacement continues to increase, the slight rocking response does not lead to a distinct inter-brick gap on the wall; instead, the vertical displacement of the bricks is limited. As seen in Figure 6d~e, at the imposed displacements of 40mm and 50mm, the vertical displacements of most bricks are less than 3mm. Compared to the severe rocking responses observed in previous shaking table test on mortarless interlocking brick wall with rebar anchorage failure [38], this observation substantiates that the tendency of rocking in the interlocking brick wall due to its absence of vertical tensile strength can be surmounted by the tensile strength provided by properly anchored vertical rebars. It is also noted that the vertical displacement contour pattern in Figure 6d~e differs from that in Figure 6b~c. This is caused by the interaction between the rebar (marked by the black dot line in Figure 6d~e) and the bricks, which confines the movement of the bricks (to be elaborated later). Overall, without the development of significant rocking response, the interlocking keys of different bricks remain in contact with one another; mechanical interlock between bricks thereby continues to take effect, resisting the load applied by the actuator. In consequence, as shown in Figure 5, the load of the envelope keeps growing after the yield point.

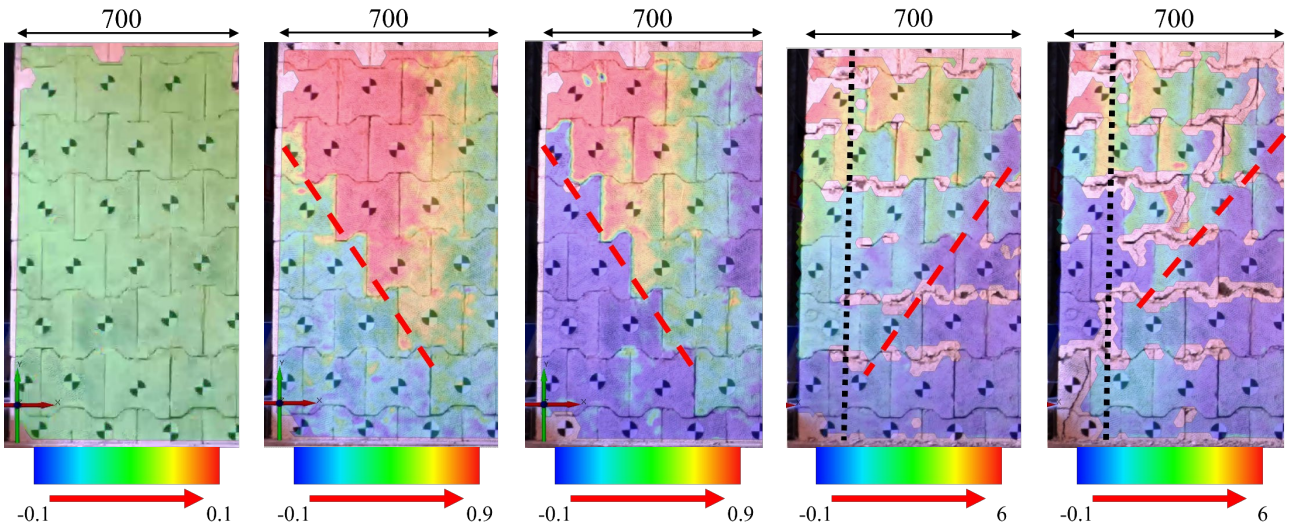

a) 0mm lateral displacement | b) 4mm lateral positive displacement | c) 10mm lateral positive displacement | d) 40mm lateral positive displacement | e) 50mm lateral positive displacement

Figure 6 Vertical displacement contours on the lower left part of the wall (unit: mm)

Figure 7 shows the damage of the bricks. No damage is observed before the applied lateral displacement reaches 40mm at which cracks initiate at the wall toes (Figure 7a~b). These cracks quickly develop upwards forming diagonal cracks (Figure 7c~d). Despite the formation of diagonal cracks, the interlocking brick wall exhibits good ductility without collapse. Similar phenomena were observed by Ingham et al. [50] and Shing et al. [51]. Using the DIC technique, the gap width variation at selected inter-brick interfaces is traced. Figure 8 shows the gap width time histories between some selected bricks. It is clearly seen that before the lateral displacement of the wall reaches 20mm, the selected gaps only have a width of around 1mm due to manufacturing imperfections. As the applied lateral displacement increases, gaps between bricks gradually increase because of brick damage. A maximum inter-brick gap opening size of about 9mm is recorded, which accounts for over 12.5% of the maximum applied lateral displacement. It should be noted that unlike conventional mortar-bonded masonry walls in which such gaps indicate bonding failure that will probably lead to wall collapse, for mortarless interlocking brick walls, the inter-brick gaps will open and close repetitively under cyclic loading while most of the interlocking keys remain intact and the interlock still takes effect. These repetitive inter-brick gap openings and closures contribute to the energy dissipation of the wall

under cyclic loading and also enhance its ductility [27, 49, 50]. Meanwhile, even for the bricks in the paths of the two major diagonal cracks, only one or two interlocking keys are damaged in most bricks, as seen in Figure 7e~f. The interlock from the remaining keys, together with the confinement from the vertical reinforcing bars, helps to prevent the wall from disintegration after the formation of major diagonal cracks [50, 52]. Therefore, despite the damage along the major diagonal cracks, most interlocking bricks are still in close contact with each other to resist the applied lateral loads. As shown in Figure 7g, local brick damages in the form of brick splitting, interlocking key abrasion or interlocking key fractures are observed in regions away from the major diagonal shear cracks on the wall, which demonstrates the participation of those interlocking bricks in resisting the lateral load. At 70mm lateral displacement, the leftmost reinforcing bar suddenly ruptures under the combined effect of the tensile force and the shear force, which abruptly releases the confinement to the wall on the left part, resulting in quick increase of the gaps between bricks and hence the drop of the loading capacity. Overall, it can be seen that the mortarless interlocking brick wall with reinforcements exhibits a shear-dominant ultimate failure mode featured by major diagonal cracks.

It should be noted that vertical reinforcement plays an important role in the mortarless interlocking brick wall. Firstly, vertical reinforcement provides vertical tensile strength for the dry-stacking interlocking brick wall which otherwise has no vertical tensile resistance due to the mortarless construction. Proper anchorage of these vertical reinforcement also effectively mitigates rocking response and thus the shear resistance of interlocking bricks can be fully activated. Secondly, the vertical reinforcements could provide confinement and thus improve the strength of the wall. They could also effectively reduce the excessive deformation and residual displacement of the wall when the bricks experience major damages.

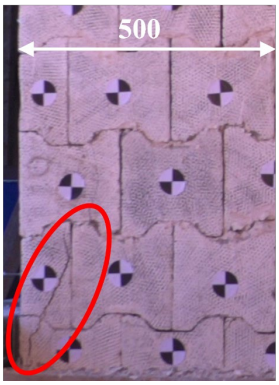

a) Left toe cracking at 40mm lateral displacement

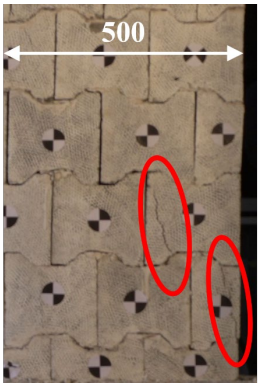

b) Right toe cracking at 40mm lateral displacement

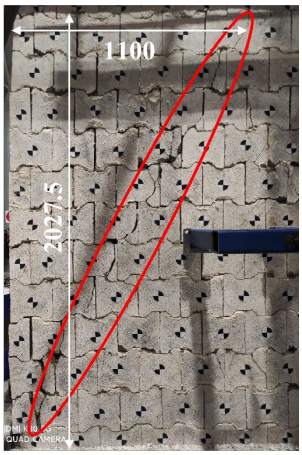

c) Diagonal crack on the left of the wall at 50mm lateral displacement

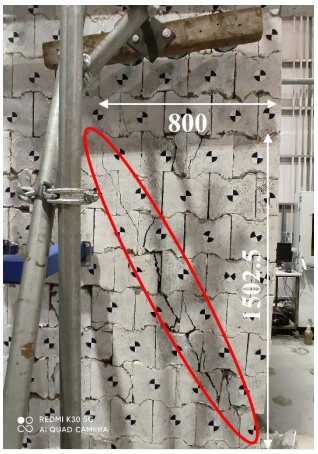

d) Diagonal crack on the right of the wall at 50mm lateral displacement

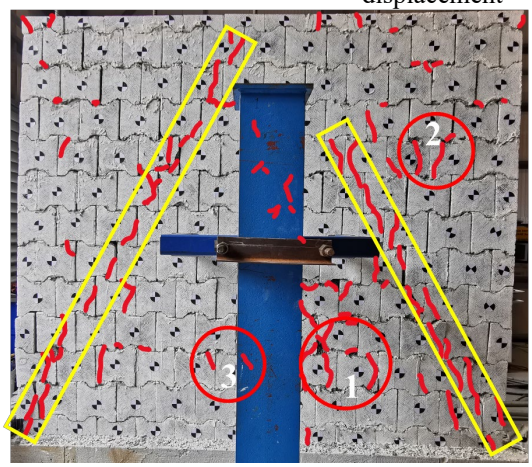

e) Ultimate failure mode of the wall on the front

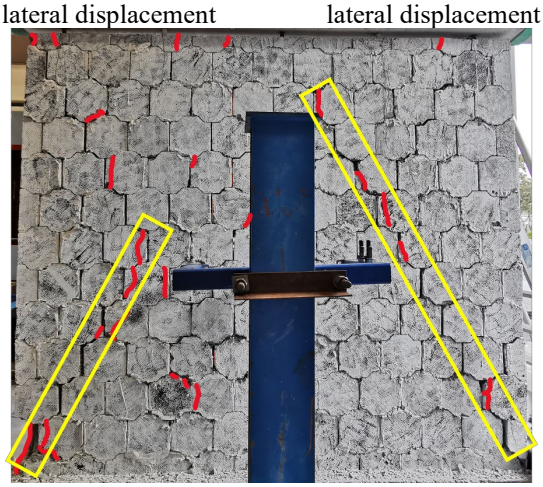

f) Ultimate failure mode of the wall on the rear

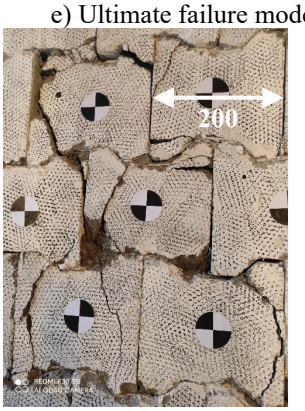

①

②

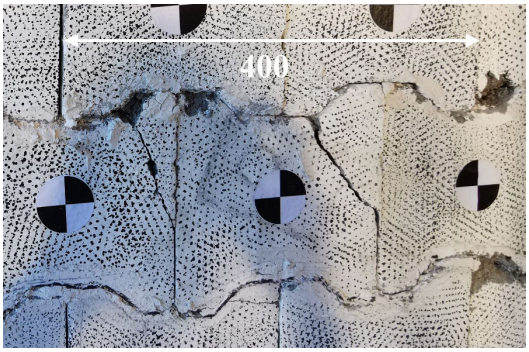

③

g) Local brick damage in areas away from the major diagonal cracks (their locations on the wall are noted with the same numbers in Figure 7e)

Figure 7 Progressive wall damages (unit: mm)

249

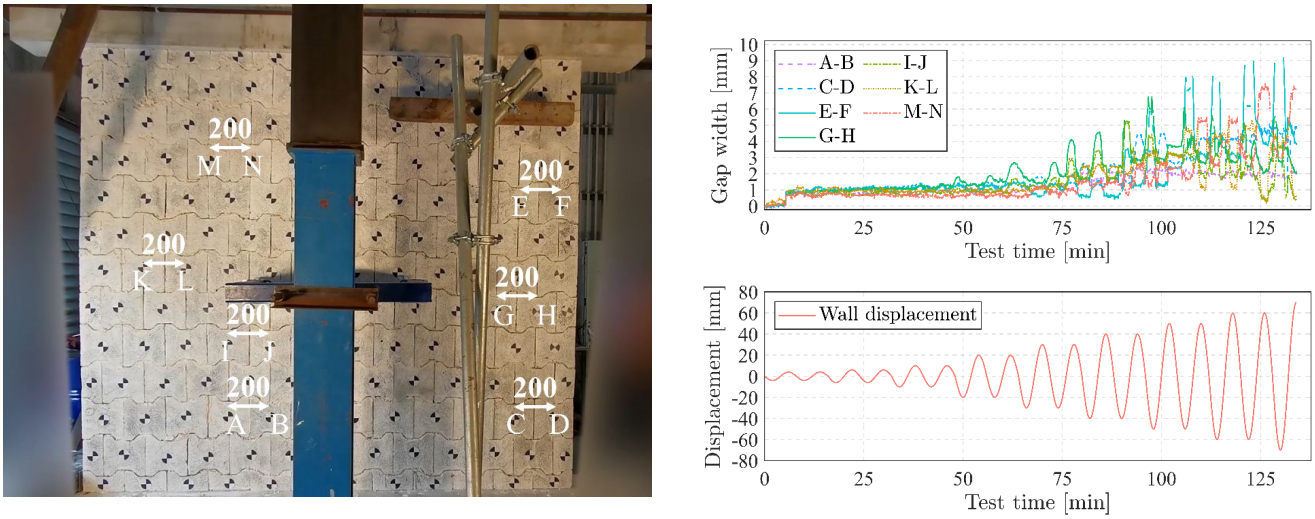

a) Gap labels (unit: mm) b) Gap width variation through the test

Figure 8 Gap width variation between selected bricks during the test

3.3 Energy dissipation

To evaluate the energy dissipation capacity of the interlocking brick wall under cyclic loading, the equivalent damping ratio ξ_{eq} is calculated with Equation (1):

$$\xi_{eq} = \Delta E_{hyst} / (2\pi E_{el}) \quad (1)$$

where the energy dissipated in each cycle ΔE_{hyst} equals to the area of the specific hysteresis loop; the elastic strain energy E_{el} is calculated as the product of the maximum displacement and the corresponding force in the cycle [53].

Figure 9 shows the calculated equivalent damping ratio of the interlocking brick wall versus the applied lateral displacement. An equivalent damping ratio of 30.9% is calculated when the applied lateral displacement is 4mm. The equivalent damping ratio decreases with the lateral displacement. At a lateral displacement of 20mm, the equivalent damping ratio decreases to 20.3%, which further decreases to 13.9% when the displacement is 70mm. Nevertheless, even when the wall eventually fails, the equivalent damping ratio is still larger than 10%, which is the minimum damping ratio requirement for reinforced masonry structures [54, 55]. The degradation of the equivalent damping ratio is caused by the reduction of friction

between interlocking bricks due to the abrasion of brick interfaces under repetitive sliding and gap opening between bricks. As reported by Liu et al. [19], the friction coefficient between interlocking bricks with rectangular or trapezoidal keys reduced by over 30% after 32 cycles of lateral loading under an axial load of 0.05MPa. With a larger axial precompression (0.47MPa) and more severe inter-brick movement in this study, the degradation of friction coefficient between bricks is more apparent and rapid.

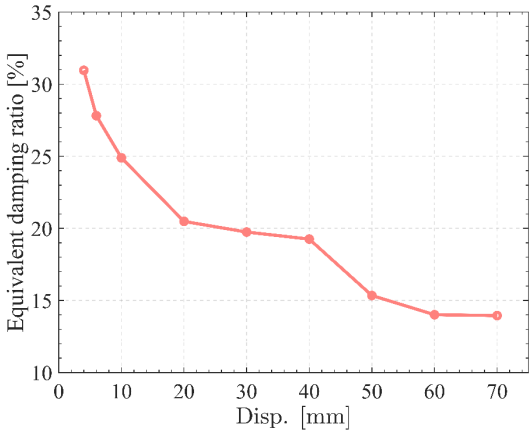

Figure 9 Equivalent damping ratio variation

It should be noted that usually the equivalent damping ratio of a structure increases with damage since the energy absorption of those structures, e.g., conventional masonry walls, relies on the material plastic deformations. For mortarless interlocking brick walls, although brick damage also contributes to energy absorption, inter-brick movements dominate the energy absorption of the wall through friction between and rocking of the bricks [38]. The friction between bricks reduces with repetitive sliding and gap opening between bricks, leading to reduction in the equivalent damping ratio of the interlocking brick wall.

4 Comparison with Conventional Masonry Walls

Comparison is made between interlocking brick wall and conventional masonry wall under cyclic loading. The cyclic performance of a conventional masonry wall with similar dimension and test setup from literature by Dhanasekar et al. [56-59] is chosen for the comparison. The conventional masonry wall was partially grouted and reinforced with vertical reinforcement only (no horizontal reinforcement as in this study). The axial precompression load applied to this conventional brick wall was also quite close to that on the

interlocking brick wall in this study. Table 2 summarises the information of the conventional brick wall. It should be noted that difference exists in the material compressive strength between the two walls. The average compressive strength is 15.7MPa for the conventional masonry prism with grout [56], while the calculated prism compressive strength of interlocking bricks is only 8.1MPa following the authors' previous study [42].

Table 2 Comparison between interlocking brick wall and conventional brick wall

Wall name	Conventional masonry wall	Interlocking brick wall
Length (mm)	2870	2400
Height (mm)	2246	2125
Thickness (mm)	150	100
Vertical reinforcement	4N12	4N20
Vertical reinforcement class	D500N	D500N
Axial precompression (MPa)	0.5	0.47
Masonry unit compressive strength (MPa)	40	20
Masonry prism compressive strength (MPa)	15.7	8.1
Dominant failure mode	Diagonal shear cracking	Diagonal shear cracking

4.1 Comparison of failure modes

Figure 10 compares the failure modes of the two walls, where the locations of vertical reinforcement bars are indicated in black lines. For the conventional wall, the diagonal cracks are in a "> <" pattern, which leads to the eventual failure of the wall. The damage is primarily formed in the two side segments of the wall between the side and central rebars, while the central wall segment between the two central rebars is relatively intact. In contrast, on the mortarless interlocking brick wall, major diagonal cracks are developed from the toes of the wall diagonally upwards. More diffused cracks can be found, which indicates the interlocking keys help to spread cracks and retard the failure of the wall (as described in Section 3.2).

It is also noticed in Figure 10a that a large proportion of the diagonal cracks on the conventional masonry wall are mortar-bonding failures, which lead to the stepped pattern of the diagonal cracks. This type of cracking is common in conventional masonry walls and shows the heterogeneity of conventional masonry and their local weakness in the bonding interfaces [60], which cause poor structural performance as well as low material efficiency [61]. In comparison, on the interlocking brick wall without mortar bonding, the cracks go through the interlocking bricks (Figure 10b). This is because the interlocking keys provide a stronger

connection between bricks, which helps to improve the efficiency of the materials in the interlocking brick wall.

a) The conventional masonry wall [56] b) The interlocking brick wall

Figure 10 Comparison of the failure modes

4.2 Comparison of the hysteresis responses

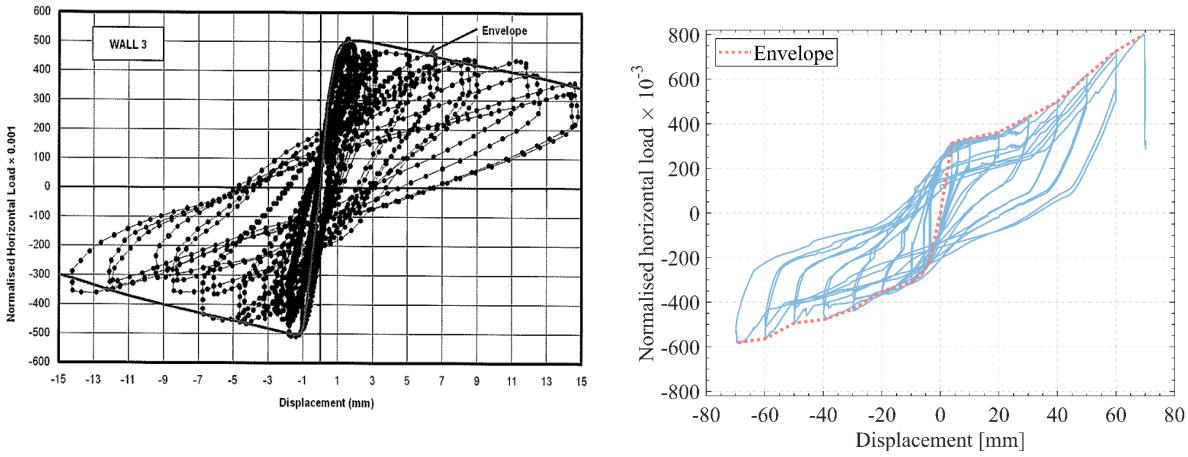

a) The conventional masonry wall [57] b) The interlocking brick wall

Figure 11 Comparison of the hysteresis response

Figure 11 compares the hysteresis response of the two walls. In Dhanasekar et al.'s study [56-59], the measured lateral loads of the walls are normalised via Equation (2) to eliminate the differences of material strength among different walls, where $\overline{V}$ is the normalised lateral load; V is the original lateral load; $f_m^{'}$ is

307 the masonry prism compressive strength in Table 2; A_g is the gross cross-sectional area of the wall. The same
308 normalisation is applied to the lateral load of the mortarless interlocking brick wall for a fair comparison.

309 $$\overline{V} = \frac{V}{\left(0.22\sqrt{f_m^{'}}\right)A_g} \quad (2)$$

310 As shown in Figure 11, the normalised peak load of the mortarless interlocking brick wall is
311 considerably larger than that of the conventional masonry wall. The mean normalised peak load is 691 for the
312 interlocking brick wall, while that of the conventional masonry wall is 510 [59], reflecting a -26.2% difference.
313 Considering that the two walls are slightly different in aspect ratio, axial precompression, vertical
314 reinforcement, etc., this comparison is made only in a broad sense. It does not mean the shear strength of the
315 studied interlocking brick wall is definitely higher than that of its conventional masonry counterpart.
316 More significant differences can be seen on the deformation capacity of the two walls. On the
317 conventional masonry wall, the yield strength was reached at 1.1mm lateral displacement in the pushing
318 direction and 0.8mm in the pulling direction, and its peak strength was reached in both directions at around
319 1.5mm [57]. Afterwards, the wall strength began to decline. The ultimate displacement (defined as the
320 displacement where the wall strength decreased to 80% of the peak strength) was 11mm in the pushing
321 direction and 8.8mm in the pulling direction, respectively [57]. The drift ratio at its peak strength was only
322 0.07%, and the averaged ultimate drift ratio was only 0.44%. In comparison, the interlocking brick wall
323 reaches its yield strength due to the slight rocking response at 4mm; after that its strength continues to increase
324 with a lower stiffness till it reaches the displacement of 70mm. The drift ratio at its peak strength is 3.29%,
325 which is 47 times that of the conventional masonry wall. The comparison demonstrates that the studied
326 interlocking brick wall has better deformation capacity than the conventional masonry wall under cyclic
327 loading. This is because: 1) as shown in Figure 8, non-negligible inter-brick sliding occurs in the mortarless
328 interlocking brick wall, which increases wall deformation without significant material damage. Secondly, as

discussed in Section 3.2 and 4.1, wall strength degradation is only observed after the wall experiences wide-spread brick damages. Under relatively low imposed lateral displacement, minor cracking and limited shear key damages are observed in the toe areas and along the diagonal struts; thus, the wall only experiences limited minor damage.

Additionally, despite the lack of energy dissipation data of the conventional masonry wall, it can be seen in Figure 11a that the hysteresis loops are narrow before the wall reaches the peak strength, indicating a poor energy dissipation capability. This is a result of the brittle nature of conventional masonry walls, where there is little material damage and interface sliding to consume the imposed energy before bonding failure occurs. In contrast, the hysteresis loops of the interlocking brick wall is relatively plump at relatively low lateral displacement (Figure 11b), denoting a much better energy dissipation capacity due to the wide-spread inter-brick sliding and rocking (Figure 8) as well as brick damage (Figure 7a~g).

Overall, from the above comparison, it is seen that before the wall starts to fail, the studied interlocking brick wall is featured with wide distribution of brick damage while the conventional mortar-bonded masonry wall is featured with concentrated mortar-bonding failures. The lateral strength of the two types of walls is comparable, but the interlocking brick wall has a larger deformation capacity and a higher energy dissipation capacity due to its ability to tolerate inter-brick movements and its better integrity owing to the interlocking mechanism.

5 Numerical Modelling

Numerical modelling is performed to assist the analyses of the response of the studied interlocking brick wall under cyclic loading.

5.1 Model details

A detailed finite element model of the mortarless interlocking brick wall is established using the commercial software Abaqus [62]. Each interlocking brick is meshed with a mesh size of 15mm after a

convergence study, as shown in Figure 12a~d. There are 1296 solid elements in each brick. It is noted that the round holes in the actual brick (Figure 1b) are simplified into square holes whose side length equals the diameter of the round holes in the brick model (Figure 12d) for a better mesh quality. It has been demonstrated by previous numerical studies that such a simplification has a minimum influence on the accuracy of the global responses of the wall [38, 63]. The three-dimensional eight-node reduced-integration element, C3D8R, is adopted for the bricks. The reinforcing bars are explicitly modelled with the three-dimensional beam element (15mm mesh size) based on the Timoshenko beam theory, B31 [64]. The cross section of the wall model is depicted in Figure 12e.

As no cohesion exists between bricks, the Coulomb friction model with a friction coefficient of 0.7 is chosen for the tangential contact between bricks [65], while the "hard" contact, which only transmits compressive force and provides no force when the two contacting surfaces separate, is set for the normal direction [64]. Similarly, as mentioned in Section 2.2, the rebars are not grouted. Therefore, the rebars are not bonded but may be in contact with the surrounding bricks during the cyclic loading test. The contact between the bricks and the reinforcement bars is also modelled with the "hard" contact in the normal direction and Coulomb friction in the tangential direction. The friction coefficient between bricks and rebars is set as 0.57 following Rabbat and Russell [66]. It should be noted that the solid element meshes are locally refined around the simplified square holes of the brick, as shown in Figure 12e.

To save computational resource and improve modelling efficiency, the top concrete beam and the bottom concrete footing are not explicitly modelled. Instead, all the degrees of freedom of the bottom nodes of the wall are restrained to simulate the fully fixed boundary condition. On the top surface of the wall, the nodal displacements, including those of the bricks and the rebars, are slaved to a reference point "O" by using the kinematic coupling method in Abaqus [62, 64]. The axial load is modelled by a downward vertical force applied on point O. To accurately model the shear span of the wall (H_0), the reference point O is set at 375mm

above the wall, which is the same height as that of the actuator in the test. This modelling scheme is illustrated in Figure 12f. In total, the model is composed of 189,784 elements and 275,948 nodes.

Following the test procedure, two-step loading phases are set for the numerical simulation, namely the static axial loading step and the subsequent quasi-static cyclic loading step. Dynamic relaxation [67] is employed in the initial axial loading step. Mass scaling is used to accelerate the computation. To ensure computation stability, the kinetic energy of the entire model is maintained to be less than 5% of its internal energy [64, 68].

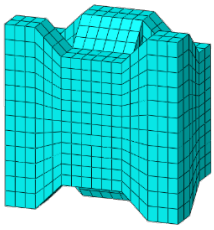

a) Brick mesh – front view

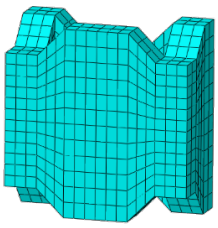

b) Brick mesh – back view

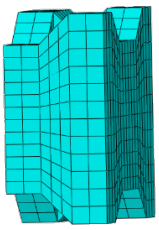

c) Brick mesh – left view

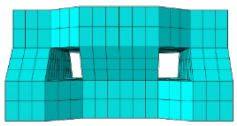

d) Brick mesh – top view (perspective)

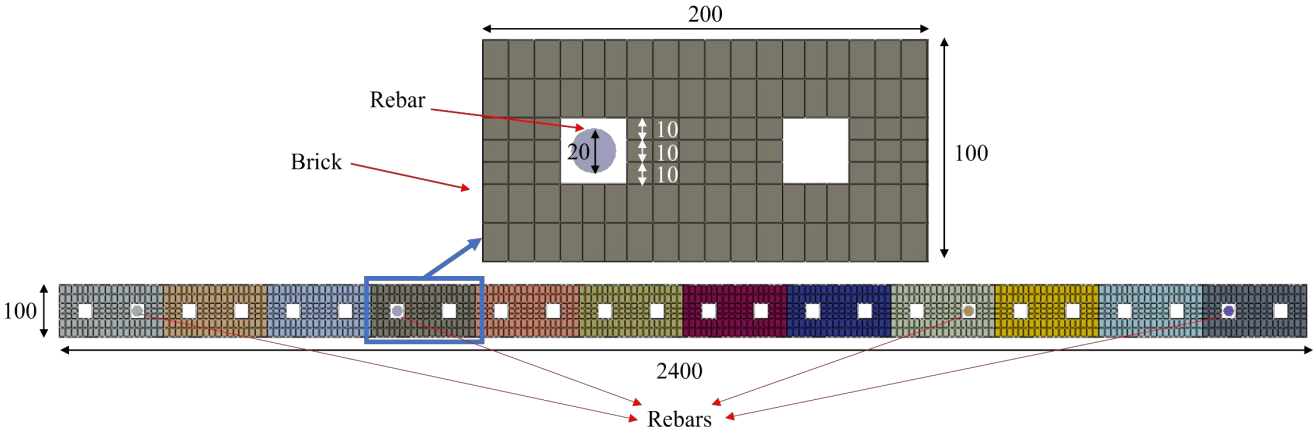

e) Cross section of the wall model (unit: mm)

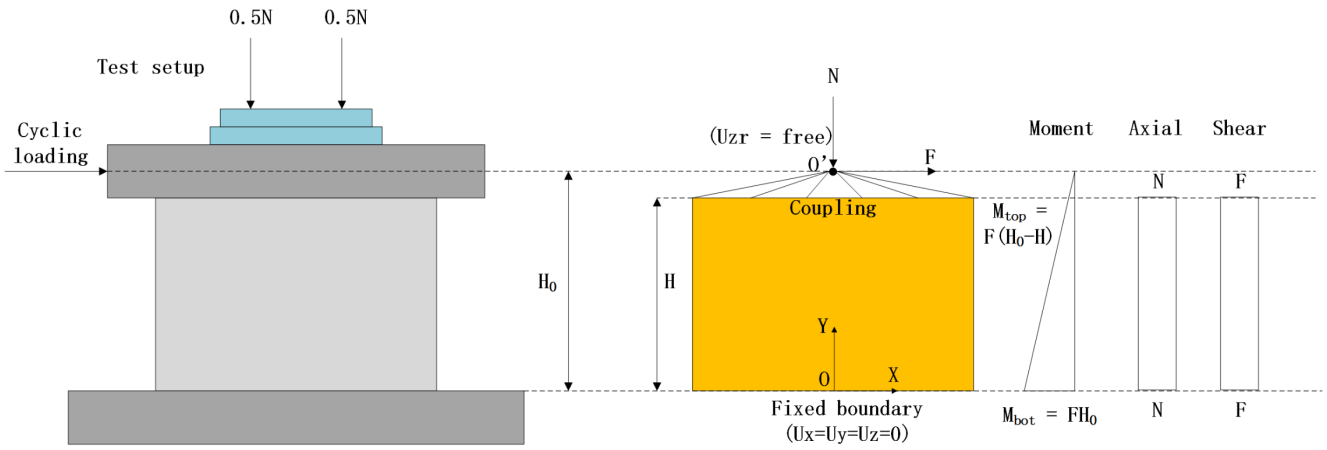

f) Simplification of the wall model

Figure 12 Numerical model of the testing wall

5.2 Material models

The damaged plasticity material model, developed by Lubliner [69] and Lee and Fenves [70], is employed for the brick material [64]. Based on the smeared cracking approach, the damaged plasticity model takes the cracked solid as a continuum and describes the cracks by stress-strain relations [71]. Therefore, it obeys the continuum assumption of the finite element method (FEM) and eliminates the need to model potential cracking [72, 73]. Additionally, a scalar stiffness degradation variable d, which is defined by Equation (3), is included in the damaged plasticity model to account for the stiffness degradation that will occur in materials under cyclic loading, where E_0 is the original Young's modulus when the material is undamaged, while E is the Young's modulus after material damage. Previous studies have demonstrated its accuracy in modelling interlocking bricks [38, 42, 63].

$$E = (1-d)E_0 \tag{3}$$

The dilation angle, the flow potential eccentricity, the ratio of initial equi-biaxial compressive yield stress to initial uniaxial compressive yield stress (σ_{b0}/σ_{c0}), and the ratio of the second stress invariant on the tensile meridian to that on the compressive meridian (K_c) are used to define the inelastic behaviour. The yield condition and the flow potential are calculated accordingly [69, 70]. Those inelasticity parameters as well as

397 the Poisson's ratio in this simulation are obtained from previous studies [74-76], which are summarised in
398 Table 3 (the density and Young's modulus are obtained from tests conducted on the brick material, as
399 mentioned in Section 2.1). These parameters prove to yield good simulation results that match well with the
400 test results.

401 Table 3 Material parameters for the damaged plasticity model of the brick material [74-76]

Density (kg/m^3)	Poisson's ratio	Young's modulus (MPa)	Dilation angle (°)	Flow potential eccentricity	$\sigma_{b0} / \sigma_{c0}$	K_c
2400	0.2	6700	30	0.1	1.16	0.6667

402

403 The stress-strain curves of the brick material are generated following the concrete design code [77, 78]
404 but based on parameters obtained from material tests in this study, i.e., the Young's modulus, the strength and
405 the corresponding strain (Section 2.1). The compressive stress-strain relation is given in Equation (4).

406
$$\sigma = \left(1 - d_c^{'}\right) E\varepsilon$$
$$d_c^{'} = \begin{cases} 1 - \dfrac{\rho_c n}{n - 1 + x^n}, x \le 1 \\ 1 - \dfrac{\rho_c}{\alpha_c \left(x - 1\right)^2 + x}, x > 1 \end{cases} \quad (4)$$
$$x = \frac{\varepsilon}{\varepsilon_c}, \rho_c = \frac{f_c}{E\varepsilon_c}, n = \frac{E\varepsilon_c}{E\varepsilon_c - f_c}, \alpha_c = 0.157 f_c^{0.785} - 0.905$$

407 where E, f_c and ε_c are the Young's modulus, the compressive strength and the compressive strain
408 corresponding to the compressive strength, respectively. Other parameters are all intermediate parameters
409 calculated from these basic parameters.

410 The tensile stress-strain relation is shown in Equation (5).

$$\sigma = (1-d_t^{'})E\varepsilon$$

$$d_t^{'} = \begin{cases} 1-\rho_t\left[1.2-0.2x^5\right], x \le 1 \\ 1-\dfrac{\rho_t}{\alpha_t\left(x-1\right)^{1.7}+x}, x > 1 \end{cases} \quad (5)$$

$$x = \frac{\varepsilon}{\varepsilon_{t,r}}, \rho_t = \frac{f_{t,r}}{E\varepsilon_{t,r}}, \alpha_t = 0.312 f_{t,r}^2$$

where f_t and ε_t are the tensile strength and the tensile strain corresponding to the tensile strength, respectively. Other parameters are also calculated from these parameters.

The scalar stiffness degradation variable d is a function of the damage parameters [64]. The damage parameters are calculated based on the stress-strain relations with the strain energy loss method [55]. As displayed in Figure 13, define the area between the ideal elastic stress-strain curve and the strain axis as S_e and the one between the real stress-strain curve and the strain axis as S_r, which can be obtained through Simpon's integration. The compressive damage parameter D_c and the tensile damage parameter D_t can then be calculated according to Equation (6).

$$D_c \text{ or } D_t = 1-\frac{S_r}{S_e} \quad (6)$$

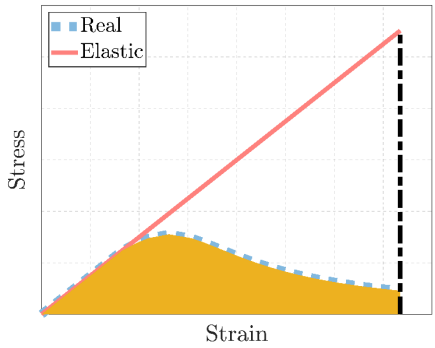

Figure 13 Calculation of damage parameters in damaged plasticity model

For the reinforcement, a bilinear stress-strain relation is adopted [79]; the material parameters are summarised in Table 4.

Table 4 Material parameters of reinforcing steel [79]

Density (kg/m^3)	Poisson's ratio	Young's modulus (MPa)	Yield strength (MPa)	Ultimate strength (MPa)	Ultimate strain
7850	0.3	200000	550	660	0.095

5.3 Model validation

To validate the accuracy of the numerical model, it is used to model the interlocking brick wall under cyclic loading presented in Section 2. The modelling results are compared with the experimental results.

Figure 14 compares the hysteresis curves from the numerical modelling and the laboratory test. A reasonably close match can be observed. It is noticed that discrepancy exists in the negative part of the hysteretic curve corresponding to the condition that the wall is subjected to pushing. As discussed in Section 3.1, this is because of the asymmetric damage of the wall in the test due to brick imperfections, which nevertheless could not be captured by the numerical model. The numerical model is able to predict the ultimate load as well as its corresponding displacement and the stiffness in each loop.

Table 5 summaries and compares the peak lateral loads at each loading cycle from the numerical modelling and the laboratory test. It can be seen that the numerical model could reasonably replicate the lateral resistance capacity of the interlocking brick wall under each prescribed lateral displacement with the largest difference about 12%. The energy dissipation capacities of the wall predicted by the numerical model and obtained from the test, i.e., the areas of the loops at different displacement levels, are summarised in Table 6. It is noted that when the imposed lateral displacement is less than 10mm, the difference of the dissipated energy between test and simulation is large. This is because the bricks in the test inevitably have imperfections due to manufacture tolerance, which introduce some pre-existing gaps in the tested wall. Even with low imposed displacements, the bricks in the tested wall can slide within those gaps and dissipate energy. Such frictional energy dissipation due to pre-existing gaps cannot be replicated in the simulation where geometrically ideal bricks are used. As the imposed lateral displacement increases, inter-brick sliding gradually occurs where there are no pre-existing gaps due to the mortarless feature and dissipates significant

amount of energy; brick material damage also develops and contributes considerably to energy dissipation. Thus, the percentage of energy dissipation by inter-brick sliding on those pre-existing gaps to the total energy dissipation becomes less pronounced. Therefore, the energy dissipation amount becomes closer between the test and the simulation with the increasing lateral displacement. As seen in Table 6, after 30mm imposed displacement, the energy dissipation differences between the test and the simulation are within 20%. After 60mm imposed displacement, the difference of the total dissipated energy between the test and the simulation is within 10%. Overall, the numerical model is capable of replicating the cyclic behaviour of the tested wall in both strength and energy dissipation.

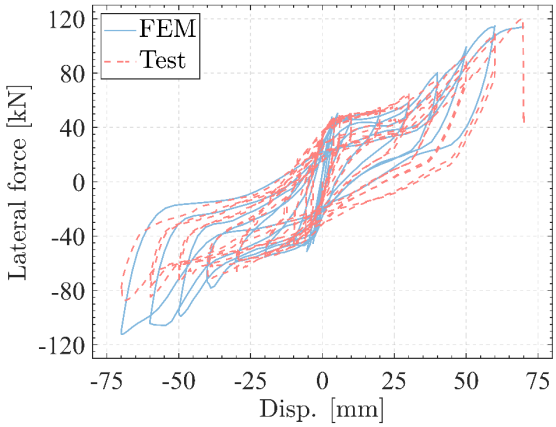

Figure 14 Comparison of hysteresis curves

Table 5 Comparison of the peak lateral load in each cycle between test and simulation in the positive direction

Displacement	Test	Simulation	Difference
4mm	44.7kN	46.7kN	4.47%
6mm	46.3kN	50.4kN	8.86%
10mm	47.4kN	46.8kN	-1.27%
20mm	52.7kN	46.3kN	-12.14%
30mm	63.8kN	58.7kN	-7.99%
40mm	73.3kN	80.4kN	9.69%
50mm	90.6kN	99.3kN	9.60%
60mm	105.4kN	114.8kN	8.92%
70mm	119.9kN	114.4kN	-4.59%

Table 6 Comparison of the dissipated energy between test and simulation

Displacement	Test	Simulation	Difference
4mm	299J	55 J	-81.61%
6mm	443 J	111 J	-74.94%

10mm	711 J	497 J	-30.10%
20mm	1341 J	995 J	-25.80%
30mm	2331 J	1903 J	-18.36%
40mm	3139 J	2611 J	-16.82%
50mm	3610 J	3178 J	-11.97%
60mm	4620 J	4388 J	-5.02%
70mm	5478 J	5916 J	8.00%

Figure 15 compares the damage of the interlocking brick wall from the numerical modelling and the laboratory test. The material stiffness degradation (SDEG) variable of the brick material is used to depict the brick damage. As shown in Figure 15a, when the wall is subjected to 40mm lateral displacement, brick damage initiates from the right-hand side toe of the wall while the rest of the wall remains intact. The numerical model well predicts the localised damage of the wall at the same displacement. When the interlocking brick wall eventually fails, shear cracks are developed in the wall after damage initiated at the toes extends upwards and diagonally. The numerical model captures a similar failure mode of the wall as in the laboratory test (Figure 15b~c), where both toe damages and diagonal cracks can be observed.

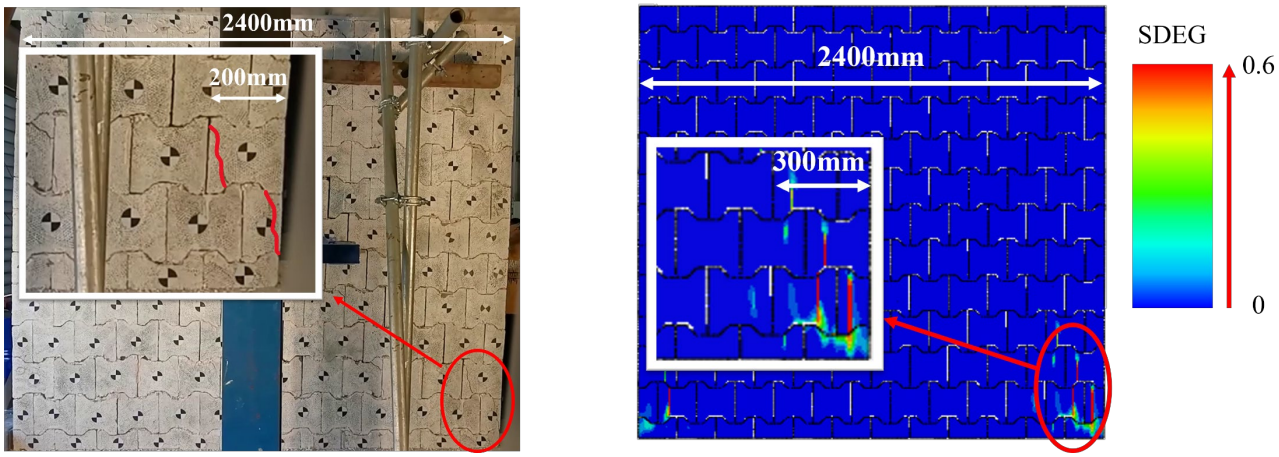

a) At 40mm lateral displacement

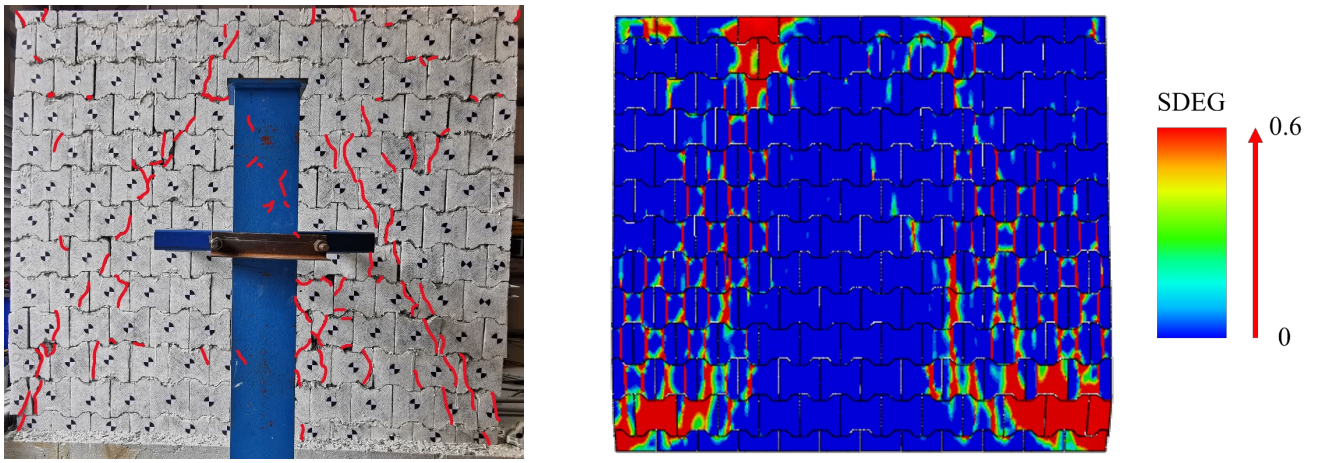

b) At 70mm wall displacement – whole wall

1) Left toe 2) Right toe

c) At 70mm wall displacement – toe areas

Figure 15 Comparisons of wall damages from laboratory test and numerical modelling

As discussed in Section 3.2, the wall experiences slight rocking response at relatively low displacements. In the numerical model, the rocking behaviour can be depicted in a more straightforward way, i.e., by showing the contact pressure (CPRESS) between bricks. Figure 16a~b show the contact pressure contours of the wall at 0mm and 4mm lateral displacement, respectively. The initial contact pressure is evenly distributed when the wall is not subjected to any lateral displacement. At 4mm lateral displacement, the contact pressure is concentrated in the upper right half of the wall with little contact pressure in the lower left part (Figure 16b). The change of contact pressure distribution denotes that even under such a low lateral displacement (4mm), the bricks in the lower left part of the wall will lose contact with one another due to slight rocking response as a result of the lack of vertical tensile strength between the mortarless interlocking

bricks. This slight rocking or lifting-up response of bricks can be observed more clearly in Figure 16c, where distinct gaps can be seen.

The above comparisons demonstrate that the developed numerical model could capture the responses of the interlocking masonry wall under cyclic loading and provide good predictions of its response and capacity.

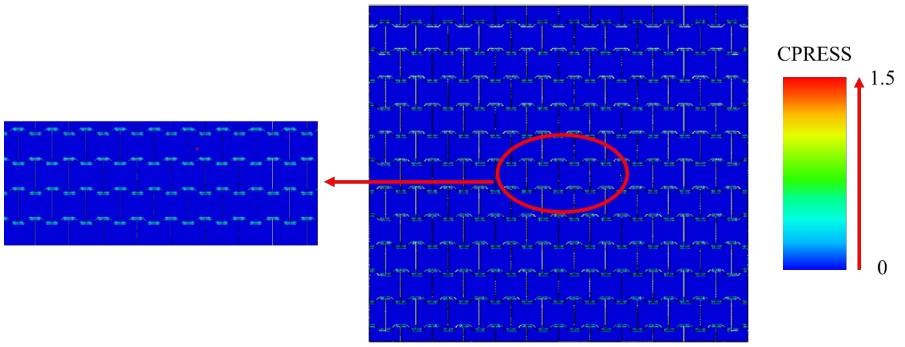

a) At 0mm displacement

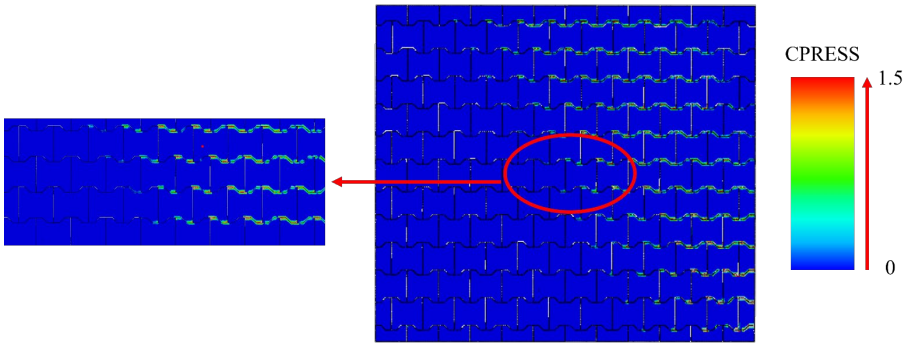

b) At 4mm displacement

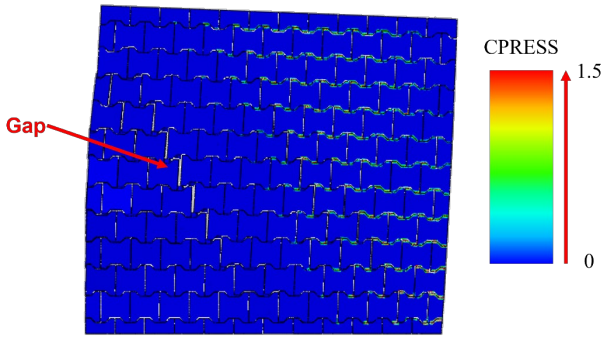

c) At 4mm displacement (deformation scale factor = 20)

Figure 16 The contact pressure distribution of the wall at 0 and 4mm lateral displacements

6 Discussions

Previous studies found that the shear span (effective height)-to-wall length ratio and the axial precompression applied to the wall could both significantly influence the shear strength and deformation capacity of conventional masonry walls [17, 80]. Numerical modelling is performed using the model validated in Section 5.3 to study the influences of these two factors on the lateral strength, ductility, energy dissipation capacity and residual displacements of mortarless interlocking brick walls under cyclic loading.

6.1 Influence of axial precompression

To investigate the influence of axial precompression on the cyclic performance of the studied interlocking brick wall, two numerical models with varying precompression levels, i.e., 0.47MPa and 0.705MPa (as listed in Table 7), are generated. The length, height and thickness of the wall are 2400mm, 2125mm and 100mm, respectively. The studied interlocking bricks are used with the material compressive strength of 20MPa and Young's modulus of 6700MPa, the same as in the test.

Table 7 Interlocking brick walls with varying axial precompressions

Case number	Axial compression (MPa)	Wall length (mm)	Wall height (mm)	Shear span (mm)	Shear span-to-wall length ratio
P1	0.470	2400	2125	2500	1.04
P2	0.705	2400	2125	2500	1.04

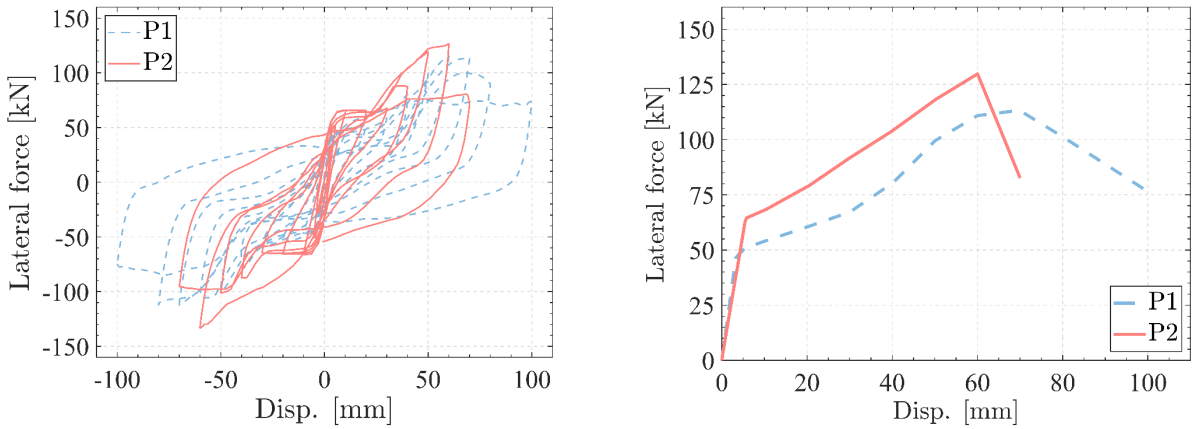

a) Hysteresis curves

b) Backbone curves

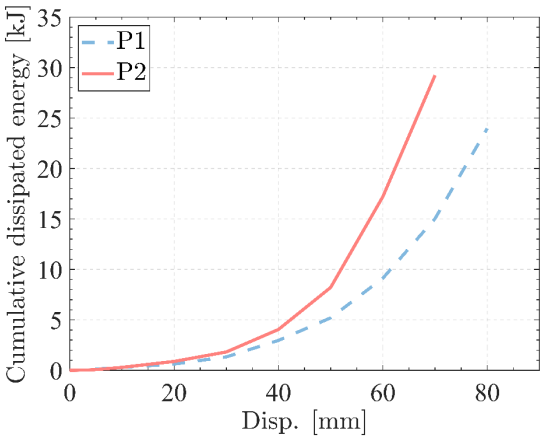

c) Cumulative energy

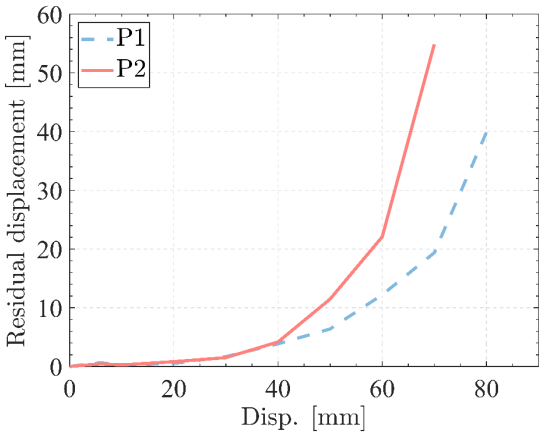

d) Residual displacement

Figure 17 Simulation results of the models with different precompressions

Figure 17a and b show the hysteresis curves and the backbone curves. The initial stiffness does not appear to vary with the level of precompression, but the ultimate strength of the wall increases with the precompression; meanwhile the ductility of the wall decreases. When the wall is under the precompression of 0.47MPa (P1), the ultimate strength is 114.4kN at the displacement of 70mm. When the precompression increases to 0.705MPa, the ultimate strength increases to 129.8kN, which is 13.5% higher than that of P1. Nonetheless, the displacement at the ultimate strength decreases to 60mm. Then, an abrupt strength degradation occurs; when the displacement reaches 70mm, the strength drops to 82.6kN, 27.8% lower than the peak strength. In comparison, for wall P1, when the displacement increases from 70mm to 80mm, the strength only degrades by 12.3% to 100.3kN. Overall, a larger axial precompression leads to a higher ultimate strength but a smaller ductility of the mortarless interlocking brick wall. Similar trends were observed on conventional masonry walls [50, 51, 81]. The strength enhancement under a larger axial precompression is mainly ascribed to the higher friction and a larger shear strength of the interlocking keys [63, 82].

Figure 17c compares the cumulative energies dissipated by the two interlocking brick walls under different axial precompression levels. With a higher axial precompression level, more cumulative energy is consumed. For example, after the 60mm-displacement cycles when the strength of wall P2 starts to degrade,

513 the cumulative dissipated energy is 17.21kJ, while only 9.13kJ energy is dissipated in wall P1, which is merely
514 53% that of P2. This is because a higher axial precompression leads to a larger frictional force and hence a
515 more considerable frictional energy dissipation. On the other hand, the larger normal precompression and the
516 larger tangent frictional forces result in larger principal stresses in the bricks of wall P2, which induce greater
517 brick damage; hence, the energy dissipated by material damage is also larger. Furthermore, the more severe
518 brick damage also increases the residual displacements in wall P2 than in P1, which is mainly a result of the
519 more severe plastic deformation of bricks. As shown in Figure 17d, before 40mm lateral displacement, the
520 residual displacements of the two walls are close to each other because the brick damage is limited; after
521 40mm imposed displacements, the residual displacements of wall P2 increases at a much higher rate than that
522 of wall P1. Under 70mm imposed displacement, wall P2 fails, while wall P1 reaches its ultimate strength; the
523 residual displacement of P2 is 54.86mm, which is almost 3 times that of wall P1 (19.37mm).

524 Through the above comparison, it can be concluded that a larger axial precompression leads to a larger
525 shear strength and a more considerable energy dissipation capacity of the studied mortarless interlocking brick
526 wall but reduces its deformation capability, and results in more severe brick damage and larger residual
527 displacements of the wall.

528 **6.2 Influence of shear span-to-wall length ratio**

529 Unlike the idealized fixed-fixed or cantilever boundary conditions, in engineering practise, walls are
530 connected by horizontal elements such as slabs and spandrels, which results in various stiffness in the top
531 boundary of the wall and thus different shear spans. Therefore, shear span-to-wall length ratio is often
532 investigated to quantify the performance of masonry walls with different boundary conditions. To study the
533 influence of shear span-to-wall length ratio on the response of the studied interlocking brick wall under cyclic
534 loading, three numerical models of the interlocking brick wall with different shear span-to-length ratios are
535 generated by changing the distance between the aforementioned point O and the top of the wall (Figure 12e).
536 As tabulated in Table 8, the same wall as above with the axial compression of 0.47MPa is modelled. The shear

span varies between 1750mm and 3125mm, corresponding to shear span-to-length ratios of 0.73 to 1.30 for the three walls. Thereby, under the same lateral force, the moment at the bottom of the wall in S2 is 25% larger than in S1, while for S3, it is 30% smaller than in S1.

Table 8 Information of models with different shear spans

Case number	Axial compression p (MPa)	Wall length L (mm)	Wall height H (mm)	Shear span H_0 (mm)	Shear span-to-length ratio H_0/W
S1	0.47	2400	2125	2500	1.04
S2	0.47	2400	2125	3125	1.3
S3	0.47	2400	2125	1750	0.73

Figure 18 a and b show the hysteresis curves and the backbone curves of the three walls with different shear spans. It is clearly seen that the ultimate strength decreases with the increase of the shear span-to-wall length ratio, while the ductility of the wall improves. In wall S3 (with a shear span-to-length ratio of 0.73), the ultimate strength is 149.6kN at the displacement of 50mm. The strength degrades rapidly with wall lateral displacement, to 128.4kN at 60mm (a decrease of 14.2%) and 79.8kN at 70mm (a decrease of 46.7% compared to the peak strength), denoting a rather brittle failure. For wall S1 with a shear span-to-length ratio of 1.04, the ultimate load is 114.4kN at the displacement of 70mm. However, distinct strength degradation occurs afterwards with a decrease of 12.3% to 100.3kN at 80mm and then a further decrease of 34.2% to 75.3kN at 100mm. Compared to that of wall S3, the ductility of wall S2 is relatively better. The ultimate strength of S2 with a shear span-to-width ratio of 1.3 is significantly lower, which has a peak strength of 81.5kN at 50mm. Nevertheless, the variation of the strength from 37mm (78.8kN, 3.3% lower than the peak strength) to 70mm wall lateral displacement (78.5kN, 3.7% lower than the peak strength) is small. This relatively stable loading capacity with wall lateral displacement in a wide range (Figure 18b) indicates the wall has a substantially better ductility. Overall, a larger shear span-to-length ratio leads to a lower shear strength but a higher deformation capacity of the mortarless interlocking brick wall. The strength reduction due to the larger shear span-to-length ratio coincides with the conventional masonry walls as specified in several masonry design

558 codes [83-85]. This is because a larger shear span-to-length ratio induces a larger sectional moment, which
559 causes more severe compressive damage on the wall and hence lowers its shear strength. The higher ductility
560 under a larger shear span-to-length ratio coincides with the results obtained from cyclic tests on conventional
561 masonry walls [86]. This is because of the larger flexural deformation as a result of the larger sectional moment
562 on walls owing to larger shear span-to-length ratios.

563 Figure 18c shows the cumulative dissipated energies calculated from the area of each hysteresis loop.
564 With the lowest shear span, the wall S3 displays the highest energy dissipation capacity. At an imposed lateral
565 displacement of 50mm, when wall S3 reaches its peak strength, the cumulative dissipated energy is 11.8kJ. In
566 comparison, the cumulative dissipated energies are both about 5.2kJ for wall S1 and S2 at this displacement,
567 which are only about 50% that of wall S3. After the imposed displacement exceeds 50mm, more significant
568 amount of energy is dissipated by wall S1 than S2. At 80mm imposed lateral displacement, the cumulative
569 dissipated energy by wall S1 is 24kJ, while that by wall S2 is 38.3% lower (14.8kJ). Wall S3 absorbs more
570 energy at the same wall displacement than the other two walls because of the more severe damage to bricks,
571 which contributes to energy absorption.

572 As displayed in Figure 18d, the residual displacements of wall S3 are remarkably larger than those of
573 the other two. After S3 reaches its ultimate strength at 50mm lateral displacement, the residual displacement
574 is 15.6mm, which is nearly 1/3 of the applied displacement, while the residual displacements of wall S1 and
575 S2 are similar (about 12mm) when the wall lateral displacement is 60mm. Afterwards, wall S1 shows larger
576 residual displacements. At 70mm lateral displacement, the residual displacement in wall S1 increases to about
577 19.4mm after it reaches its ultimate strength, which further increases to 39.9mm when the imposed lateral
578 displacement is 80mm. In contrast, when wall S2 is subject to 70mm and 80mm lateral displacements, the
579 residual displacements are 17.3mm (10.9% lower than that of S1) and 24.3mm (39.1% lower than that of S1),
580 respectively. The lower residual displacements of S2 are ascribed to the larger contribution of flexural wall

deformation to its total deformation due to its higher shear span. As observed by Magenes and Calvi [49], a flexure-dominant wall tends to show a low residual displacement.

Through the above comparison, it can be concluded that decreasing the shear span-to-wall length ratio of a mortarless interlocking brick wall will lead to a higher shear strength, a lower ductility, a larger energy dissipation capacity and more pronounced residual displacements.

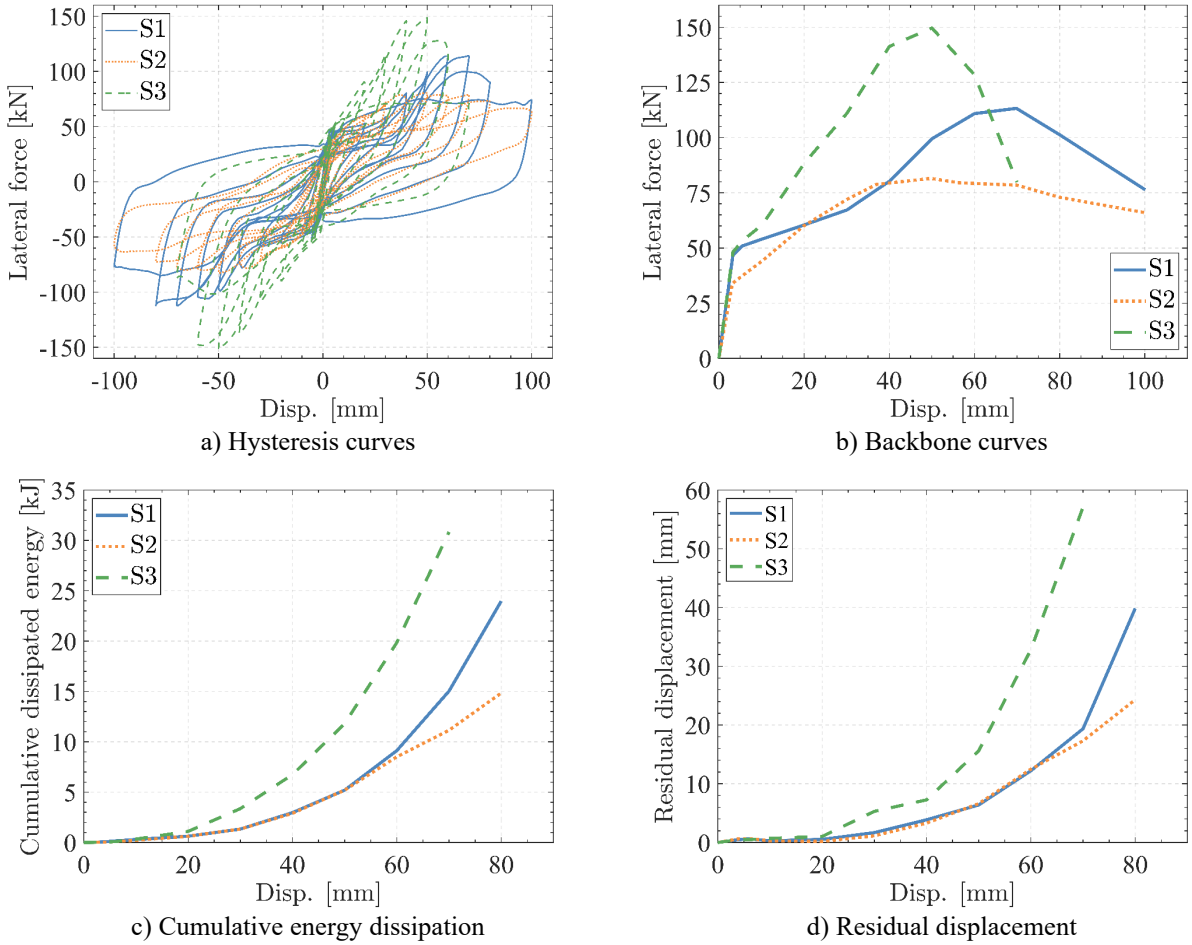

a) Hysteresis curves

b) Backbone curves

c) Cumulative energy dissipation

d) Residual displacement

Figure 18 Simulation results of the models with different shear span-to-length ratios

7 Conclusions

This paper presents experimental and numerical studies on the cyclic behaviour of mortar-less interlocking masonry walls made of a specific type of bricks with large interlocking keys. A laboratory in-plane cyclic test is conducted to assess the damage mode, hysteresis response and energy dissipation capacity of the mortarless

590 interlocking brick wall. The test results are compared with those of a conventional masonry wall in literature
591 on the failure modes, shear strength and ductility. A detailed numerical model is established and validated
592 with the laboratory testing results. The influences of the axial precompression force and shear span-to-length
593 ratio on the performance of interlocking brick walls are numerically investigated. The following conclusions
594 are obtained:

595 1. Under in-plane cyclic loading, the interlocking brick wall firstly experiences slight rocking and sliding
596 response between bricks at a relatively low imposed lateral displacement because of the mortarless
597 construction method. However, strong anchorage through vertical reinforcing bars restrains the further
598 development of rocking response in the wall. Under further increased lateral displacement, the
599 interlocking brick wall suffers diagonal shear dominated cracking damage.
600 2. Because of the outstanding shear resistance provided by the large interlocking keys, the interlocking brick
601 wall exhibits good shear resistance. Considerable deformation capability is observed on the interlocking
602 brick wall due to the inter-brick movement.
603 3. An initial equivalent damping ratio of over 30% is calculated on the interlocking brick wall, which
604 gradually decreases under cyclic loading due to the abrasion of brick surfaces. The equivalent damping
605 ratio maintains at over 10% before the ultimate failure of the wall.
606 4. Comparison between the conventional masonry wall and the mortarless interlocking brick wall
607 demonstrates the latter has a higher shear strength and a larger deformation capability. The large
608 interlocking keys and the mortarless construction method eliminate the bonding failure which is
609 commonly observed in conventional masonry walls. Hence, a better material efficiency can be achieved
610 in the mortarless interlocking brick wall.
611 5. Through numerical modelling, it is found that increasing the axial precompression or decreasing the shear
612 span-to-length ratio will enhance the ultimate strength and energy dissipation capability, but reduce the

deformation capability and lead to more severe damage and larger residual displacements of the studied mortarless interlocking brick wall.

Overall, the laboratory test and numerical simulation developed in this research provide insights into the seismic performance of mortarless interlocking brick walls made of interlocking bricks with large shear keys. It demonstrates good potential to be used in seismic regions. Future study can be focused on further quantifying the influence of different design parameters on the seismic performance of the wall and developing analytical models for efficient evaluations of the wall.

8 Acknowledgements

The authors would like to acknowledge the financial support from Australian Research Council (ARC) under grant ID DE210100986 for conducting this study.

References

[1] D'Amato M, Laterza M, Diaz Fuentes D. Simplified Seismic Analyses of Ancient Churches in Matera's Landscape. International Journal of Architectural Heritage. 2020;14:119–38.
[2] Fuentes DD, Laterza M, D'Amato M. Seismic Vulnerability and Risk Assessment of Historic Constructions: The Case of Masonry and Adobe Churches in Italy and Chile. In: Aguilar R, Torrealva D, Moreira S, Pando MA, Ramos LF, editors. Structural Analysis of Historical Constructions. Cham: Springer International Publishing; 2019. p. 1127–37.
[3] Ramírez E, Lourenço PB, D'Amato M. Seismic Assessment of the Matera Cathedral. In: Aguilar R, Torrealva D, Moreira S, Pando MA, Ramos LF, editors. Structural Analysis of Historical Constructions. Cham: Springer International Publishing; 2019. p. 1346–54.
[4] Fallahi A. Lessons Learned from the Housing Reconstruction Following the Bam Earthquake in Iran. The Australian Journal of Emergency Management. 2007;22:26–35.
[5] Oyguc R, Oyguc E. 2011 Van Earthquakes: Lessons from Damaged Masonry Structures. Journal of Performance of Constructed Facilities. 2017;31:04017062.
[6] Sun B, Yan P, Hu C, Zhang M. Overview on seismic damage to different structures in Yingxiu Town during Wenchuan Earthquake. Journal of Earthquake Engineering and Engineering Vibration. 2008;28:1–9.
[7] Wang G, Li Y, Zheng N, Ingham JM. Testing and modelling the in-plane seismic response of clay brick masonry walls with boundary columns made of precast concrete interlocking blocks. Engineering Structures. 2017;131:513–29.
[8] Ramamurthy K, Kunhanandan Nambiar EK. Accelerated masonry construction review and future prospects. Progress in Structural Engineering and Materials. 2004;6:1–9.
[9] Peirs G. Masonry in the third millennium. In: West HWH, British Masonry S, editors. Masonry (8): British Masonry Society; 1998. p. 6–8.

[10] Yong HTD. Utilisation of topologically-interlocking osteomorphic blocks for multi-purpose civil construction. Perth, Western Australia: The University of Western Australia; 2011.
[11] Ali M, Gultom RJ, Chouw N. Capacity of innovative interlocking blocks under monotonic loading. Construction and Building Materials. 2012;37:812–21.
[12] Gul A, Alam B, Shahzada K. Seismic performance evaluation of unconfined dry stacked block masonry structure. Engineering Structures. 2022;265.
[13] Fay L, Cooper P, Morais HFd. Innovative interlocked soil–cement block for the construction of masonry to eliminate the settling mortar. Construction and Building Materials. 2014;52:391–5.
[14] Ben Ayed H, Limam O, Aidi M, Jelidi A. Experimental and numerical study of Interlocking Stabilized Earth Blocks mechanical behavior. Journal of Building Engineering. 2016;7:207–16.
[15] Uzoegbo HC. Lateral Loading Tests on Dry-Stack Interlocking Block Walls. Structural Engineering, Mechanics and Computation2001. p. 427-36.
[16] Thomas J. Technical Details. Bellevue WA: Tetraloc Pty Ltd.; 2019.
[17] Dolatshahi KM, Nikoukalam MT, Beyer K. Numerical study on factors that influence the in-plane drift capacity of unreinforced masonry walls. Earthquake Engineering & Structural Dynamics. 2018;47:1440–59.
[18] Sturm T, Ramos LF, Lourenço PB. Characterization of dry-stack interlocking compressed earth blocks. Materials and Structures. 2015;48:3059–74.
[19] Liu H, Liu P, Lin K, Zhao S. Cyclic Behavior of Mortarless Brick Joints with Different Interlocking Shapes. Materials (Basel, Switzerland). 2016;9.
[20] Lin K, Liu HJ, Totoev YZ. Lateral bearing capacity and simplified equations of dry-stack in-filled reinforcement concrete frame structure. J Civ Archit Environ Eng. 2013;35:21–7.
[21] Lin K, Liu HJ, Totoev YZ. Quasi-static experimental research on dry-stack masonry infill panel frame. J Build Struct. 2012;33:119–27.
[22] Ahmed A, Afreen A, Moin K. State of Art Review: Behaviour of Masonry Structures under Gravity and Seismic Loads. International Journal of Emerging Technology and Advanced Engineering. 2017;7:202–14.
[23] Ferretti E, Pascale G. Some of the Latest Active Strengthening Techniques for Masonry Buildings: A Critical Analysis. Materials (Basel, Switzerland). 2019;12.
[24] Ferreira TM, Costa AA, Costa A. Analysis of the Out-Of-Plane Seismic Behavior of Unreinforced Masonry: A Literature Review. International Journal of Architectural Heritage. 2015;9:949–72.
[25] Gupta P, Sankhla SS. A Review Study on Performance of Stone Masonry Building Under Earthquake. International Journal of Advance Engineering and Research Development. 2018;5:45–50.
[26] Magenes G, PENNA A. Seismic design and assessment of masonry buildings in Europe: recent research and code development issues. In: Ingham JM, Dhanasekar M, Masia M, editors. Proceedings of the 9th Australasian Masonry Conference. Auckland, N.Z.: Australasian Masonry Conference; 2011.
[27] Bland DW. In-Plane Cyclic Shear Performance of Interlocking Compressed Earth Block Walls. San Luis Obispo, California: California Polytechnic State University; 2011.
[28] Qu B, Stirling BJ, Jansen DC, Bland DW, Laursen PT. Testing of flexure-dominated interlocking compressed earth block walls. Construction and Building Materials. 2015;83:34–43.
[29] Kohail M, Elshafie H, Rashad A, Okail H. Behavior of post-tensioned dry-stack interlocking masonry shear walls under cyclic in-plane loading. Construction and Building Materials. 2019;196:539–54.
[30] Gul A, Alam B, Khan IU, Shah SAA, Khan SW, Shahzada K. Improving seismic capacity of dry stacked interlocking masonry structure through confinement at corners. Soil Dynamics and Earthquake Engineering. 2023;165.
[31] Zhang X, Hao H, Li C, van Do T. Experimental study on the behavior of precast segmental column with domed shear key and unbonded Post-Tensioning tendon under impact loading. Engineering Structures. 2018;173:589–605.

692 [32] Zhang X, Hao H, Zheng J, Hernandez F. The mechanical performance of concrete shear key for
693 prefabricated structures. Advances in Structural Engineering. 2021;24:291–306.
694 [33] Zhang X, Hao H, Li C. The effect of concrete shear key on the performance of segmental columns
695 subjected to impact loading. Advances in Structural Engineering. 2017;20:352–73.
696 [34] Elvin A, Uzoegbo HC. Response of a full-scale dry-stack masonry structure subject to experimentally
697 applied earthquake loading. Journal of the South African Institution of Civil Engineering. 2011;53:22–32.
698 [35] Elvin A. Experimentally applied earthquakes and associated loading on a full-scale dry-stacked masonry
699 structure. Journal of the South African Institution of Civil Engineering. 2009;51:15–26.
700 [36] Ali M. Use of coconut fibre reinforced concrete and coconut-fibre ropes for seismic-resistant construction.
701 Materiales de Construcción. 2016;66:e073.
702 [37] Ali M, Briet R, Chouw N. Dynamic response of mortar-free interlocking structures. Construction and
703 Building Materials. 2013;42:168–89.
704 [38] Xie G, Zhang X, Hao H, Bi K, Lin Y. Response of reinforced mortar-less interlocking brick wall under
705 seismic loading. Bulletin of Earthquake Engineering. 2022;20:6129-65.
706 [39] Xie G, Zhang X, Hao H, Thomas J. Response of Mortar-Free Interlocking Brick Wall under Seismic
707 Excitation. Proceedings of 2020 Australian Earthquake Engineering Society Conference. Virtual: Australian
708 Earthquake Engineering Society; 2020. p. 309–16.
709 [40] Dyskin AV, Pasternak E, Estrin Y. Mortarless structures based on topological interlocking. Frontiers of
710 Structural and Civil Engineering. 2012;6:188-97.
711 [41] Martínez M, Atamturktur S, Ross B, Thompson J. Assessing the Compressive Behavior of Dry-Stacked
712 Concrete Masonry with Experimentally Informed Numerical Models. Journal of Structural Engineering.
713 2018;144:04018080.
714 [42] Shi T, Zhang X, Hao H, Chen C. Experimental and numerical investigation on the compressive properties
715 of interlocking blocks. Engineering Structures. 2021;228:111561.
716 [43] Howlader MK, Masia MJ, Griffith MC. In-Plane Response of Perforated Unreinforced Masonry Walls
717 under Cyclic Loading: Experimental Study. Journal of Structural Engineering. 2020;146:04020106.
718 [44] Security USDoH, Agency FEM. Interim Testing Protocols for Determining the Seismic Performance
719 Characteristics of Structural and Nonstructural Components: FEMA 461. Scotts Valley: CreateSpace
720 Independent Publishing Platform.
721 [45] Tomaževič M. Earthquake-resistant design of masonry buildings. London: Imperial College Press; 1999.
722 [46] Eurocode 8: Design of structures for earthquake resistance. Part 3, Assessment and retrofitting of
723 buildings. London: British Standards Institution; 2006.
724 [47] Housing Mo, China U-RDotPsRo. Specification for seismic test of buildings: JGJ/T 101-2015. Beijing:
725 China Architecture & Building Press.
726 [48] Doherty K, Griffith MC, Lam N, Wilson J. Displacement-based seismic analysis for out-of-plane bending
727 of unreinforced masonry walls. Earthquake Engineering & Structural Dynamics. 2002;31:833–50.
728 [49] Magenes G, Calvi GM. In-plane seismic response of brick masonry walls. Earthquake Engineering &
729 Structural Dynamics. 1997;26:1091–112.
730 [50] Ingham JM, Davidson BJ, Brammer, Voon KC. Testing and codification of partially grout-filled
731 nominally-reinforced concrete masonry subjected to in-plane cyclic loads. The masonry society journal.
732 2001;19:83–96.
733 [51] Shing PB, Schuller M, Hoskere VS. In-Plane Resistance of Reinforced Masonry Shear Walls. Journal of
734 Structural Engineering. 1990;116:619–40.
735 [52] Abdel-Hafez LM, Abouelezz AEY, Elzefeary FF. Behavior of masonry strengthened infilled reinforced
736 concrete frames under in-plane load. HBRC Journal. 2015;11:213–23.

[53] Chopra AK. Dynamics of structures: Theory and applications to earthquake engineering / Anil K. Chopra, University of California at Berkeley. Fourth edition, International edition, Global edition ed. Boston: Pearson; 2014.
[54] Huang L, Lu Y, Yan L, Kasal B, Wang L, Zhang T. Seismic performance of mortarless reinforced masonry walls. Journal of Building Engineering. 2020;31:101368.
[55] Priestley MJN, Calvi GM, Kowalsky MJ. Displacement-based seismic design of structures. Pavia: IUSS Press; 2007.
[56] Dhanasekar M, Haider W. Effect of Spacing of Reinforcement on the Behaviour of Partially Grouted Masonry Shear Walls. Advances in Structural Engineering. 2011;14:281–93.
[57] Dhanasekar M, Haider W, Janaraj T. Response of partially grouted wider reinforced masonry walls to inplane cyclic shear. In: Serega S, Winnicki A, editors. Proceedings of the 7th International Conference on Analytical Models and New Concepts in Concrete and Masonry Structures. CD Rom: Cracow University of Technology; 2011. p. 1-12.
[58] Janaraj T, Dhanasekar M, Haider W. Wider reinforced masonry shear walls subjected to cyclic lateral loading. Architecture Civil Engineering Environment (ACEE). 2011;4:39-46.
[59] Haider W. Inplane response of wide spaced reinforced masonry shear walls: Central Queensland University Australia; 2007.
[60] Celano T, Argiento LU, Ceroni F, Casapulla C. Literature Review of the In-Plane Behavior of Masonry Walls: Theoretical vs. Experimental Results. Materials (Basel, Switzerland). 2021;14.
[61] Calderon S, Vargas L, Sandoval C, Araya-Letelier G. Behavior of Partially Grouted Concrete Masonry Walls under Quasi-Static Cyclic Lateral Loading. Materials (Basel). 2020;13.
[62] Hibbitt D, Karlsson B, Sorensen P. Abaqus FEA. 2019 FD01 ed: Dassault Systèmes; 2019.
[63] Shi T, Zhang X, Hao H, Xie G. Experimental and numerical studies of the shear resistance capacities of interlocking blocks. Journal of Building Engineering. 2021;44:103230.
[64] Systèmes D. Abaqus Documentation R2022x. 2022.
[65] Chen S, Bagi K. Crosswise tensile resistance of masonry patterns due to contact friction. Proceedings of the Royal Society A: Mathematical, Physical and Engineering Sciences. 2020;476:20200439.
[66] Rabbat BG, Russell HG. Friction Coefficient of Steel on Concrete or Grout. Journal of Structural Engineering. 1985;111:505-15.
[67] Boulbes RJ. Troubleshooting finite-element modeling with Abaqus: With application in structural engineering analysis / Raphael Jean Boulbes. Cham: Springer; 2020.
[68] Lemos J. Discrete Element Modeling of the Seismic Behavior of Masonry Construction. Buildings. 2019;9:43.
[69] Lubliner J, Oliver J, Oller S, Oñate E. A plastic-damage model for concrete. International Journal of Solids and Structures. 1989;25:299–326.
[70] Lee J, Fenves GL. Plastic-Damage Model for Cyclic Loading of Concrete Structures. Journal of Engineering Mechanics. 1998;124:892–900.
[71] Rots JG, Blaauwendraad J. Crack models for concrete, discrete or smeared? Fixed, multi-directional or rotating? HERON. 1989;34.
[72] Lourenço PJBB. Computational strategies for masonry structures [PhD]. Delft, Netherlands: TU Delft; 1996.
[73] Stavridis A, Shing PB. Finite-Element Modeling of Nonlinear Behavior of Masonry-Infilled RC Frames. Journal of Structural Engineering. 2010;136:285–96.
[74] Nie Y, Sheikh A, Griffith M, Visintin P, Vaculik J. The application of mixed-mode de-cohesion criteria in masonry finite element analysis. Australian Earthquake Engineering Society 2019 Conference. Newcastle, New South Wales: Australian Earthquake Engineering Society; 2019.

[75] Al-Ahdal A, Aly N, Galal K. Simplified analytical models for partially grouted reinforced masonry shear walls. Engineering Structures. 2022;252:113643.
[76] Bui Q-B, Bui T-T, Tran M-P, Bui T-L, Le H-A. Assessing the Seismic Behavior of Rammed Earth Walls with an L-Form Cross-Section. Sustainability. 2019;11.
[77] Housing Mo, China U-RDotPso. Code for Design of Concrete Structures. Beijing: China Architecture Publishing & Media Co., Ltd.; 2016.
[78] China MoHaU-RDotPso. Code for Design of Concrete Structures. Beijing2015.
[79] Menegon SJ, Tsang HH, Wilson JL, Lam NTK. Overstrength and ductility of limited ductile RC walls: from the design engineers perspective. The Tenth Pacific Conference on Earthquake Engineering. Sydney, Australia: Australian Earthquake Engineering Society; 2015.
[80] Sandoval C, Calderón S, Almazán JL. Experimental cyclic response assessment of partially grouted reinforced clay brick masonry walls. Bulletin of Earthquake Engineering. 2018;16:3127–52.
[81] Kasparik T, Tait MJ, El-Dakhakhni WW. Seismic Performance Assessment of Partially Grouted, Nominally Reinforced Concrete-Masonry Structural Walls Using Shake Table Testing. Journal of Performance of Constructed Facilities. 2014;28:216–27.
[82] Bolhassani M, Hamid AA, Johnson C, Schultz AE. Shear strength expression for partially grouted masonry walls. Engineering Structures. 2016;127:475–94.
[83] Building code requirements and specification for masonry structures: TMS 402/602-16. Longomont: The masonry society; 2016.
[84] Design of masonry structures: CSA S304.1-14. Third edition ed. Mississauga, Ontario: CSA Group; 2014.
[85] AS 3700-2018: Masonry Structures. Sydney, N.S.W.: Standards Australia; 2018.
[86] Petry S, Beyer K. Influence of boundary conditions and size effect on the drift capacity of URM walls. Engineering Structures. 2014;65:76–88.